DEVELOPMENT OF ANALYSIS APPROACH UTILIZING EXTENDED COMMON MID-POINT METHOD TO ESTIMATE ASPHALT PAVEMENT THICKNESS WITH 3-D GPR

BY

SHAN ZHAO

THESIS

Submitted in partial fulfillment of the requirements
for the degree of Master of Science in Civil Engineering
in the Graduate College of the
University of Illinois at Urbana-Champaign, 2015

Urbana, Illinois

Adviser:

Professor Imad L. Al-Qadi

ABSTRACT

Layer thickness is a critical part of the flexible pavement system. It can affect the structural capacity of existing flexible pavement, and can be used to predict its remaining service life. For newly constructed flexible pavement, obtaining its layer thickness is essential for the purposes of quality control and quality assurance (QC/QA).

Currently, most departments of transportation, highway agencies, and consultants in the United States use destructive methods, e.g. coring, to obtain asphalt pavement layer thicknesses. As a non-destructive technique, ground penetration radar (GPR) has also been applied to estimate asphalt pavement thickness. However, the use of GPR is limited due to the difficulty involved in determining the dielectric constant of asphalt pavement in the traditional two-way travel time and surface reflection method. Asphalt mixture is a composite material and, as such, the reflection amplitude of electromagnetic waves could be affected by many factors, such as the presence of moisture. The extended common mid-point (XCMP) method is an alternative method that can be used on the traditional air-coupled pulsed horn antenna to increase the accuracy of asphalt pavement thickness estimation without calibrating the dielectric constant by taking cores. By developing signal processing and numerical analysis techniques, this research attempts to integrate 3-D GPR with the XCMP method, which holds certain advantages over the traditional air-coupled pulsed horn antenna.

3-D GPR is a multi-array stepped-frequency radar that can measure both in-line and cross-line directions at a very close sampling interval. Therefore, 3-D radar provides faster data collection speeds than the pulsed horn antenna and is preferred in large survey areas such as an airport runway/taxiway. To solve the XCMP equations, the time domain sampling rate of the 3-D

radar is increased by applying a Whittaker-Shannon interpolation. The XCMP equations are then solved numerically in the least-square sense.

By validating the developed algorithm in a full scale test site, the study concludes that by using signal processing techniques and numerical analysis approaches, 3-D radar can be used to accurately predict asphalt layer thickness using the XCMP method when the layer thickness is greater than 50mm.

ACKNOWLEDGEMENTS

I would like to first thank my advisor, Professor Imad Al-Qadi, who gave me this great opportunity to study at the University of Illinois. This thesis would not have been possible without his guidance and invaluable advice. I would also like to thank all the staff at the Advanced Transportation Research & Engineering Laboratory (ATREL) here in the Department of Civil & Environmental Engineering at the University of Illinois for providing me with timely and indispensable help. Thanks are equally due to my colleagues at ATREL.

My final and deepest acknowledgment goes to my parents, Wencai Tian and Laibin Zhao, whose love and support I treasure. Special thanks also to my family members and friends, whether in China or here in the US, for their companionship and encouragement.

TABLE OF CONTENTS

CHAPTER 1: INTRODUCTION

1.1 Background

Asphalt concrete (AC) is a composite material consisting of bituminous and aggregate, and is widely used in pavement construction. Asphalt pavement is also called "flexible pavement," as opposed to Portland cement concrete (PCC) pavement, which is also known as "rigid pavement." AC pavement typically provides a smoother drive and generates less roadway noise than its PCC counterpart (Claessen et al. 1977). Layer thickness is crucial in the asphalt pavement system, and most asphalt pavement design processes consider it to be the most important parameter (Huang 1993; Yoder et al. 1975; Masad 2012). For newly constructed asphalt pavement, layer thickness is used for quality control and quality assurance (QC/QA); for existing pavement, it is used for condition assessment of existing pavements and in predicting their remaining service life.

Predicting the layer thicknesses is, therefore, necessary whether during construction or for existing pavement. However, it still remains an issue to estimate asphalt layer thickness effectively and non-destructively. Traditionally, coring has been the prevalent method for agencies seeking to obtain asphalt layer thickness (Lahouar 2003). However, taking cores results in pavement defects; as such, the number of coring locations is usually limited. In addition, coring provides limited layer thickness information of the asphalt pavement. Ground penetrating radar (GPR) represents an alternative, non-destructive method.

GPR is a specific type of radar system that uses electromagnetic (EM) waves to explore subsurface. In transportation infrastructure survey, GPR has been commonly applied to locate reinforcement and delamination under a concrete slab (Chang et al. 2009). In flexible pavement (asphalt pavement), GPR has been used to detect free water (Al-Qadi et al. 1991), to estimate the

dielectric property of pavement materials (Al-Qadi et al. 2001), and to estimate the layer thicknesses (Al-Qadi and Lahouar 2005) and asphalt concrete layer density (Leng 2011; Leng et al. 2011; Shangguan et al. 2014a; Shangguan 2015). ASTM standard ASTM D6432-11 provides a procedure of applying GPR for subsurface investigation.

1.2 Problem statement

One of the most successful applications of GPR on flexible pavement is in estimating layer thicknesses—a job for which the two-way travel time method was traditionally employed. The dielectric property of the asphalt material was usually determined by the surface reflection method. The major limitation of this approach is that the surface reflection cannot be obtained with enough accuracy. Calibrating the dielectric constant by taking cores may improve the dielectric constant accuracy; however, this is, again, destructive, rendering the use of GPR meaningless.

Leng and Al-Qadi (2014) developed the extended common mid-point (XCMP) method, which can be used on 2GHz air-coupled pulsed horn antennas to estimate asphalt pavement thickness with high accuracy without the need of dielectric constant calibration via coring. This was an extension of the common-midpoint method introduced by Al-Qadi and his coworkers (Lahouar et al. 2002). One of the disadvantages of pulsed horn antenna is that the GPR survey is limited to a line scan. In applications where large areas need to be surveyed—e.g. an airport runway/taxi way—the GPR survey with single horn antenna can be extremely time consuming.

A new type of GPR was recently developed in Norway. The 3-D GPR contains an antenna array, which has very close sampling interval in the cross-line direction. This 3-D GPR enables data collection at much faster speeds, making it possible to efficiently survey large areas.

3-D GPR is different from an air-coupled horn antenna in many ways. These include the characteristics of the antenna, the number of channels, the way signals are generated, the gain, and the characteristics of the EM signals. For example, both the time domain sampling rate and bandwidth of the 3-D GPR are less than that of the 2GHz pulsed antenna. Since XCMP methods require very high time domain sampling rates to ensure the solution of the XCMP equations, it is necessary to develop signal processing techniques for the 3-D GPR signals to increase its own time domain sampling rate. Analytical methods are also needed to solve the XCMP equations.

1.3 Research objectives

The main objective of this research is to integrate the XCMP method with stepped-frequency 3-D GPR. As a result, large areas can be surveyed using 3-D GPR at faster speeds, and a two-dimensional thickness profile can be generated with high accuracy without the need of dielectric constant calibration via coring. In order to achieve this objective, the research efforts focus on characterizing 3-D GPR properties, developing signal processing techniques as a pre-process of the XCMP method, and developing numerical methods to solve the XCMP equations.

In order to validate the outcome of this study, four XCMP configurations were tested on a full scale test site and ground truth data were obtained. This allows the accuracy for each of the XCMP configurations to be assessed and corresponding recommendations to be proposed for the practical use of XCMP methods with 3-D GPR.

1.4 Thesis scope

This thesis has five chapters. Chapter 1 provides a brief introduction to the research and the study objectives. Chapter 2 presents the current state of knowledge on the electromagnetic theories, the fundamentals of GPR, and the GPR applications on asphalt pavement. Chapter 3 provides a detailed description of the XCMP method used in the study, the experiment plan with

the 3-D GPR, and the development of signal processing techniques needed as pre-process for XCMP method. Chapter 4 delineates and discusses the numerical results of both standard scan patterns and the four XCMP configurations. Chapter 5 summarizes the findings and conclusions based on the results from Chapter 4 and includes recommendations for future studies.

CHAPTER 2: THE CURRENT STATE OF KNOWLEDGE

2.1 Electromagnetic theory

The EM phenomenon can be described by four Maxwell's equations which relate the electric and magnetic fields to their sources. These were established by James Clerk Maxwell (1831-1879) based on experimental discoveries of Andre-Marie Ampere (1775-1836), Michael Faraday (1791-1867), and Carl Frierich Gauss (1777-1855).

The Maxwell's equations in integral forms in terms of total charges and currents are:

$$\oint_c \vec{E} \bullet d\vec{l} = -\frac{d}{dt} \iint_S \vec{B} \bullet d\vec{S} \tag{2-1}$$

$$\oint_c \vec{B} \bullet d\vec{l} = \varepsilon_0 \mu_0 \frac{d}{dt} \iint_S \vec{E} \bullet d\vec{S} + \mu_0 \iint_S \vec{J}_{total} \bullet d\vec{S} \tag{2-2}$$

$$\oiint_S \vec{E} \bullet d\vec{S} = \frac{1}{\varepsilon_0} \iiint_V \rho_{e,total} dV \tag{2-3}$$

$$\oiint_S \vec{B} \bullet d\vec{S} = 0 \tag{2-4}$$

where $\vec{E}$ is electric field intensity (Volts/meter), $\vec{B}$ is magnetic flux density (Webers/meter^2), $\vec{J}_{total}$ is electric current density (Amperes/meter^2), ε_0 =8.854*10^{-12}F/m=1/36pi*10^{-9}F/m is permittivity of free space (Farads/meter), μ_0 =4pi*10^{-7}H/m is permeability of free space (Henrys/meter), and $\vec{\rho}_{e,total}$ is electric charge density (coulombs/meter^3) in volume V.

Faraday's induction law (2-1) shows that a changing magnetic flux can generate an electric field. The Maxwell-Ampere's law (2-2) shows that an electric current or a changing electric field can generate a magnetic field. Gauss' law (2-3) pertains to static electric fields, showing that the

electric field lines originate from positive charges and terminate at negative charges. Gauss' law for magnetism (2-4) shows that magnetic flux lines don't have origins and must form a circle.

By taking account of electric polarization and magnetization effects, the Maxwell-Ampere's law (2-2) and Gauss' law (2-3) can be written in terms of free charges and currents:

$$\oint_c \vec{H} \bullet d\vec{l} = \frac{d}{dt} \iint_S \vec{D} \bullet d\vec{S} + \iint_S \vec{J}_{free} \bullet d\vec{S} \tag{2-5}$$

$$\oiint_S D \bullet d\vec{S} = \iiint_V \rho_{e,\text{free}} dV \tag{2-6}$$

where $\vec{D} = \varepsilon \vec{E}$ is the electric flux density in coulombs/meter^2, ε is called the permittivity of the material, $\vec{H} = \frac{\vec{B}}{\mu}$ is the magnetic field intensity in amperes/meter, and μ is called the permeability of the material. There will be conductive current given by $\vec{J} = \sigma \vec{E}$, where σ is the conductivity of a medium in siemens/meter.

Maxwell's Equations in the integral form are valid everywhere. However, the integral form is not convenient for analyzing physical problems. Therefore, it is necessary to convert them to the differential forms:

$$\nabla \bullet \vec{E} = 0 \tag{2-7}$$

$$\nabla \bullet \vec{H} = 0 \tag{2-8}$$

$$\nabla \times \vec{E} = -\mu \frac{\partial \vec{H}}{\partial t} \tag{2-9}$$

$$\nabla \times \vec{H} = \varepsilon \frac{\partial \vec{E}}{\partial t} \tag{2-10}$$

In this document, the pavement mediums are assumed to be homogeneous, isotropic, and non-dispersive.

In the application of GPR, the object is usually in the far field region of the antenna. In the far field of an antenna, the EM field exhibits local plane wave behavior. If we assume the EM wave is propagating in the z direction, the EM filed is linearly polarized (the most general case being elliptically polarized) with an electric field only in the x direction. Then, by solving Maxwell's equations, the harmonic plane wave solution in a lossless medium ($\sigma = 0$) can be expressed as follows:

$$\vec{E}(\mathrm{z}) = \hat{\mathrm{x}}\, E_{0x} \cos(\omega \mathrm{t} - \beta \mathrm{z}) \tag{2-11}$$

$$\vec{H}(\mathrm{z}) = \hat{y} H_{0y} \cos(\omega \mathrm{t} - \beta \mathrm{z}) \tag{2-12}$$

where E_{0x} and H_{0y} are arbitrary constant values, $Z = \frac{E_{0x}}{H_{0y}} = \sqrt{\frac{\mu}{\varepsilon}}$ is the wave impedance ω is the angular frequency, and $\beta = \omega\sqrt{\mu\varepsilon}$ is the phase constant.

Form Equations (2-11) and (2-12), the EM wave velocity can be calculated as:

$$v = \frac{\omega}{\beta} = \frac{1}{\sqrt{\mu\varepsilon}} \tag{2-13}$$

In free space, the EM wave velocity is equal to $\frac{1}{\sqrt{\mu_0 \varepsilon_0}} = 3\times 10^8 m/s$, which is the speed of light in free space.

In general, the electric permittivity and magnetic permeability of a material can be expressed as ratio relative to the permittivity and permeability of space: $\mu_r = \frac{\mu}{\mu_0}, \varepsilon_r = \frac{\varepsilon}{\varepsilon_0}$. The relative permeability and relative permittivity (or dielectric constant) are called μ_r and ε_r, respectively.

If the plane wave is normally incident on an interface of medium 1 and medium 2, the reflection coefficient *R* and transmission coefficient *T* are:

$$R = \frac{\eta_2 - \eta_1}{\eta_2 + \eta_1} \tag{2-14}$$

$$T = \frac{2\eta_2}{\eta_2 + \eta_1} \tag{2-15}$$

where $\eta_1 = \sqrt{\mu_1 / \varepsilon_1}$ and $\eta_2 = \sqrt{\mu_2 / \varepsilon_2}$ are the intrinsic impedance of medium 1 and medium 2, respectively. This is Snell's law of reflection and transmission in the normal incident case. From Equations (2-14) and (2-15), we can see if medium 1 and medium 2 are the same, then R=0 and T=1, which shows that there is no reflection. If medium 2 is a perfect conductor, then $\eta_2 = 0$, R = -1, and T = 0, meaning that all of the EM waves are flipped and reflected back.

For flexible pavement, the asphalt material can be considered non-magnetic ($\mu_r = 1$) and non-conductive ($\sigma = 0$); therefore, the only important electric property is the dielectric constant. Figure 2-10 shows a typical GPR signal reflected from a pavement system consisting of a surface layer whose dielectric constant is ε_1 and a second layer whose dielectric constant is ε_2. Tx/Rx represents the location of the monostatic antenna. A_0 and A_1 are the amplitudes of the reflection

from the surface and the bottom of the surface layer, respectively. According to Equation (2-14), the dielectric constant of the surface layer is:

$$\varepsilon_1 = \left(\frac{1+\frac{A_0}{A_p}}{1-\frac{A_0}{A_p}} \right)^2 \tag{2-16}$$

where A_p is the amplitude of the reflected signal collected over a copper plate placed on the pavement surface, which can be considered a perfect reflector.

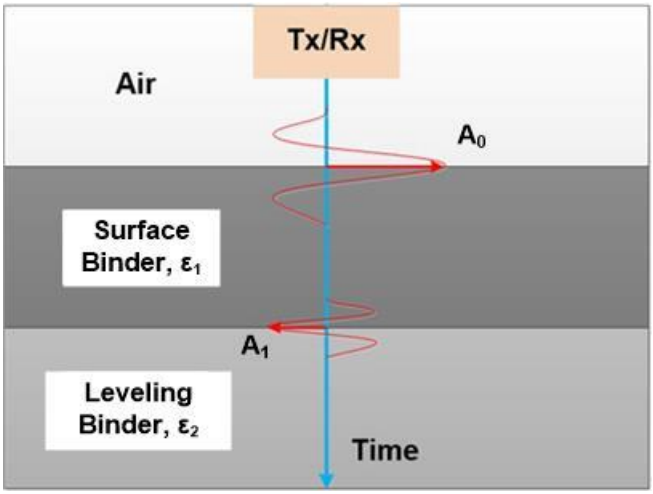

Figure 2-1. Typical GPR signal reflected from a pavement system (Zhao *et al.* 2015)

Knowing the dielectric constant of the surface layer, the thickness of the surface layer can be calculated using the two-way travel time method:

$$h = \frac{v\Delta t}{2} \tag{2-17}$$

where h is the layer thickness, Δt is the EM wave two-way travel time within the surface layer, $v = c/\sqrt{\varepsilon_r}$ is the speed of EM wave, c is the speed of light in free space ($3 \times 10^8 m/s$), and ε_r is the dielectric constant of the surface layer.

The surface reflection and two-way travel time method provide an easy way to obtain the dielectric constant of pavement and the thickness of the pavement layer. However, the reflection amplitude can easily be affected by many factors, such as the surface moisture, temperature, instability of the GPR system, and environment electric noise. Therefore, the resulting dielectric constant and layer thickness may not be accurate enough. One possible solution is to calibrate the dielectric constant of pavement: that is, take cores of pavement and back-calculate the dielectric constant with obtained two-way travel time. However, this method is destructive and not preferred. In this study, another algorithm – the common midpoint method – is used as an alternative to obtain the dielectric constant and layer thickness. This method can provide better accuracy compared to surface reflection and two-way travel time method without the need of calibration with cores.

2.2 Fundamental of GPR

Electrical signals are transmitted via transmission line or through empty space. Antennas are essentially transducers that can convert electrical signals from transmission lines to empty space, or vice versa. According to IEEE, an antenna is defined as "that part of transmitting or receiving system that is designed to radiate or to receive electromagnetic waves" (IEEE 1993). Ground penetration radar, in contrast, is a type of radar whose purpose is to locate targets or interfaces buried with earth material (Daniels 2005).

2.2.1 Air coupled horn antenna

One of the most popular GPR systems is the air-coupled system with horn antennas. Figure 2-2 shows a typical vehicle-mounted air-coupled GPR system. The two orange boxes are two horn antennas with a 2GHz central frequency, and are manufactured by Geophysical Survey Systems, Inc. (GSSI). There is a control unit called SIR20 that sends a signal to the antennas during GPR surveys. There is also a distance measuring instrument (DMI) mounted on the back wheel of the van to collect distance information or a GPS system. The GPR control unit and DMI system are shown in Figure 2-3. The air-coupled antenna allows for the collection of GPR data on pavement at highway speeds. Another advantage of this GPR system is that the horn antenna is a type of aperture antenna (i.e., an antenna that has a physical aperture through which EM waves flow) that has gains larger than 15 dB, which implies very good directivity (Stutzman and Thiele 2012).

Figure 2-2. A vehicle-mounted air-coupled GPR system

Figure 2-3. GPR system control unit – SIR20 and DMI

2.2.2 Ultra wide band bowtie antenna

Resolution describes the ability of a signal to distinguish adjacent pulses. For example, an EM wave with a shorter wavelength, or higher frequency, could distinguish objects with smaller distances; therefore a signal with higher frequency usually has a greater resolution than a low frequency signal. The Rayleigh resolution criteria, proposed by Lord Rayleigh (Culick 1987), is the most common criteria for resolution. The one dimensional Rayleigh resolution of a signal is the width of a pulse, which is defined as the distance between the maximum point of the pulse and the first zero point of the pulse. A band pass filter usually decreases the resolution of a signal.

A horn antenna usually has a moderate bandwidth, or range of operation frequency. In civil engineering applications where the target is deep, such as with ancient archeological structures, low frequency antennas are desirable, due to their larger penetration depth; while in applications at near surface levels, such as pavement inspection, higher frequency antennas are superior since they can provide a better time domain resolution. In line with this, a broadband antenna could better satisfy the requirement. A broadband antenna has a pattern, gain, and impedance nearly

constant over a wide frequency range, because it has an active region that relocates on the antenna as the frequency changes. The bowtie antenna, or the bifin antenna, is an ultra-wideband antenna yielding very fine time domain resolutions (Eide 2000). Its main beams perpendicular to the antenna plane and it is also linearly polarized. In addition to a better time domain resolution, the bowtie antenna also have finer lateral resolutions since bandwidth is the most important factor for the resolution (Jol 2008). A typical bowtie antenna is characterized by its angle between the two metal pieces, α, and the total length, L, as shown in Figure 2-4.

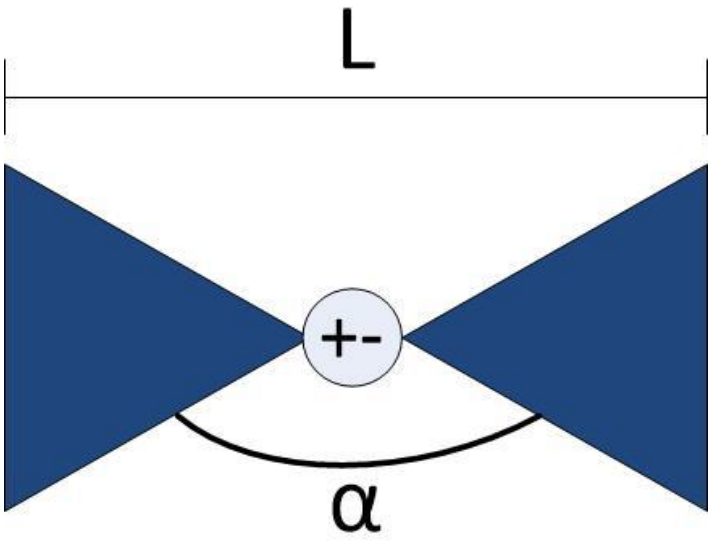

Figure 2-4. A typical bowtie antenna

2.2.3 Stepped frequency signal

Due to the constant radiation pattern over very wide frequency bands, broadband antennas such as the bowtie antenna introduced in section 2.1.2 can radiate signals at stepped frequency. Stepped frequency signals have successive pulses with linearly increasing frequency in discrete steps. As shown in Figure 2-5, the frequency increases with time by the frequency step, while the

dwell time is the duration over which each frequency is emitted. The time domain sketch of the signal is shown in Figure 2-6.

It should be noted that the stepped frequency signal is collected in the frequency domain. Specifically, the amplitude and phase of the frequency response is recorded at each frequency step by sending and receiving the corresponding harmonic waves. The time domain signal can then be retrieved by calculating the inverse Fourier transform of the frequency response.

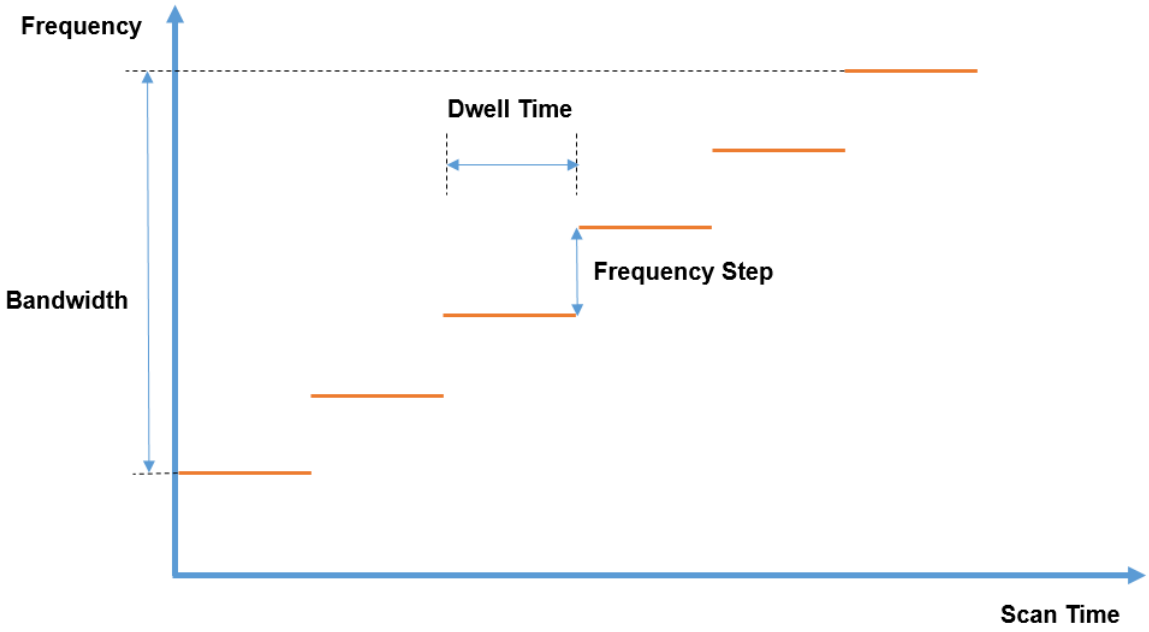

Figure 2-5. Spectrogram of stepped frequency signal

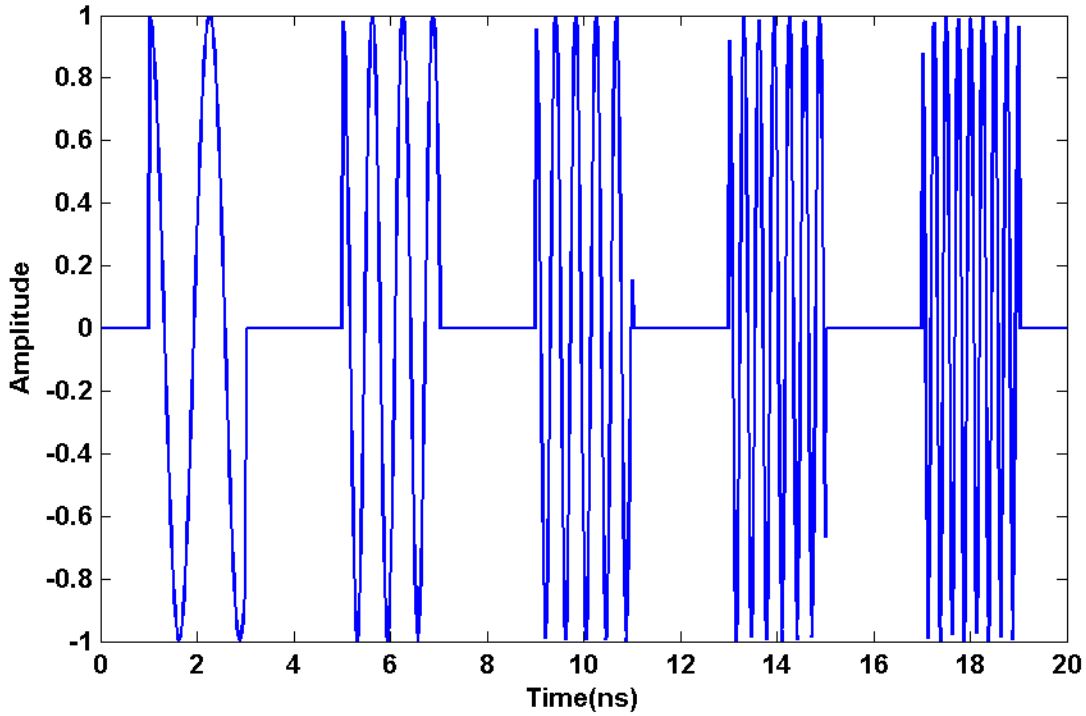

Figure 2-6. Time domain waveform of stepped frequency signal

With increased dwell time, a better signal to noise ratio (SNR) can be obtained. However, due to the long dwell time, the survey speed of a single stepped frequency system will be slower than in a pulsed system.

2.2.4 Antenna array

An antenna array is a combination of multiple antenna elements. During data collection, electric signals are simultaneously transmitted through all elements of the array, and the reflected signals are also simultaneously received by all elements of the array. The first popular antenna array was the Yagi antenna, invented in 1926 by Shintaro Uda and Hidetsugu Yagi (Uda 1925), and was widely used during World War II. Arrays are popular since, unlike a single antenna, their radiation pattern can be controlled by adjusting the spacing and phasing of each array element.

An antenna array can be characterized by the radiation pattern of a single element, i.e. the element pattern, and by the radiation pattern of the array if its actual elements are replaced by isotropic point sources. The latter is defined as the array factor. The total pattern of the array is then the product of the array factor and element pattern.

The type of array element is determined by the application of the antenna. For example, a horn antenna array can provide moderate bandwidth and need fewer array elements but the number of scans is limited due to wide element spacing. A bowtie antenna element, on the other hand, has a wide beam, simple structure, and a broad bandwith (Stutzman and Thiele 2012).

A synthetic aperture radar (SAR) is a single antenna moving from position to position, and is therefore superficially similar to an antenna array (Blahut 2004). Unlike a real antenna array, the antenna sends the pulse and records the reflection at each position one at a time. Since the antenna is transmitting and receiving while moving, the EM wave is doppler-shifted. It should be noted that a SAR can give less information than a real antenna array since it misses the information when a signal is transmitted and received by two different antenna elements.

2.2.5 3-D GPR

In 2001, a new type of GPR—3-D GPR—was developed in Norway. The major components of the 3-D GPR system are shown in Figure 2-7: an antenna array, a GeoScope control unit, an operator PC with data collection and analysis software (3DR EXAMINER), and, sometimes, a GPS. A 3-D GPR system thus consists of an array of electronically switched transmit/receive bow-tie antenna pairs ranging from 9 to 41 with the width of the antenna arrays ranging between 0.9 and 3.3m. Figure 2-8 shows the VX1821 model, which has 11 antenna pairs. The transmitter is denoted by “T” and the receiver is denoted by “R.”

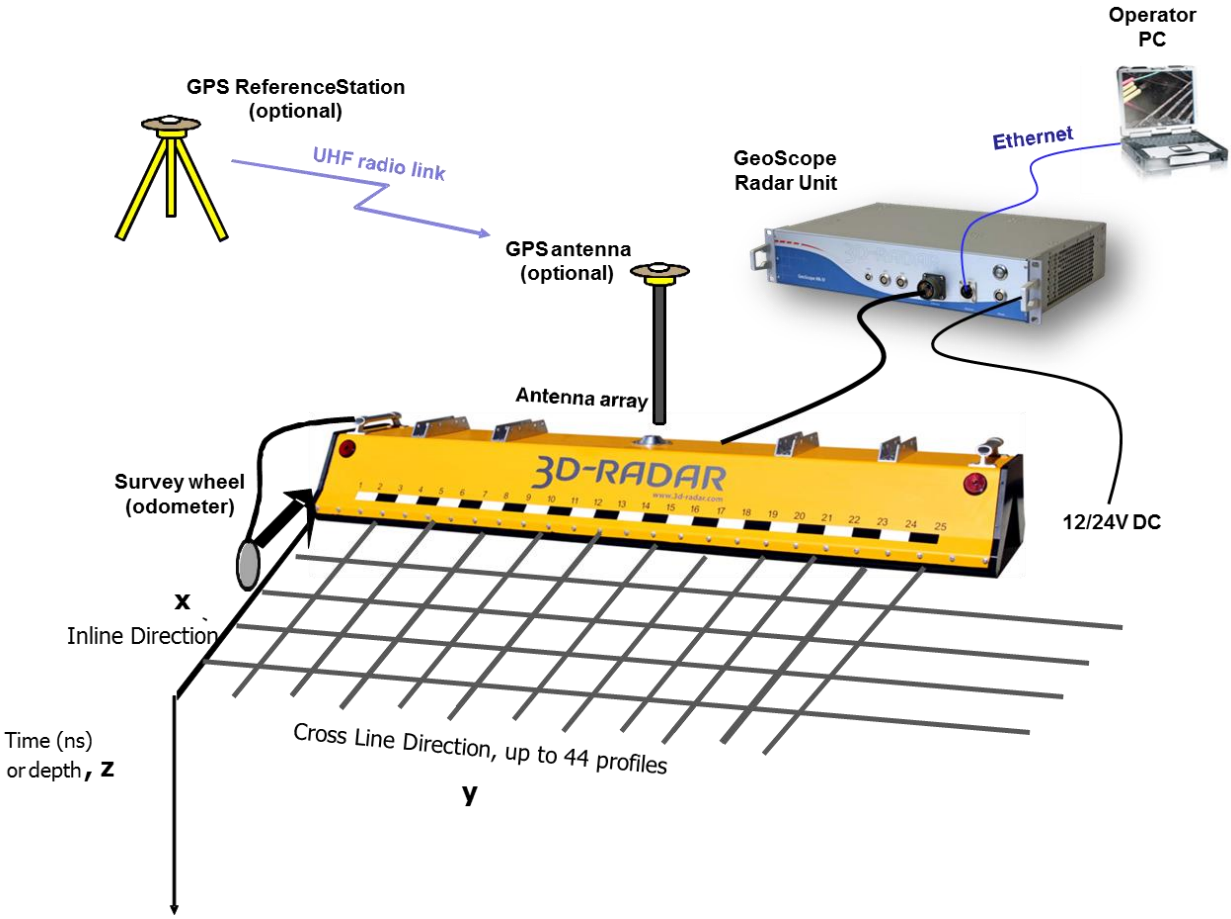

Figure 2-7. 3-D GPR system (3-D radar GPR 2015)

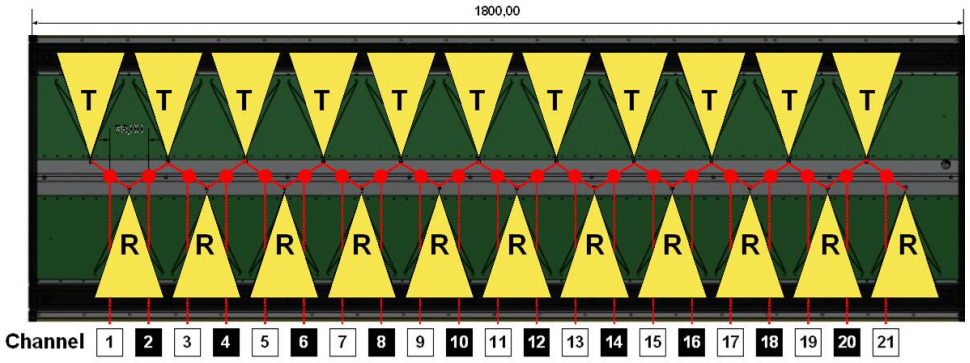

Figure 2-8. Model VX1821 antenna array (Eide and Sala 2012)

The antenna element used in the 3-D GPR is a bowtie antenna with frequency ranges from 200 MHz – 3 GHz. The simulated radiation patterns of this kind of bowtie antenna at different frequency levels are shown in Figure 2-9.

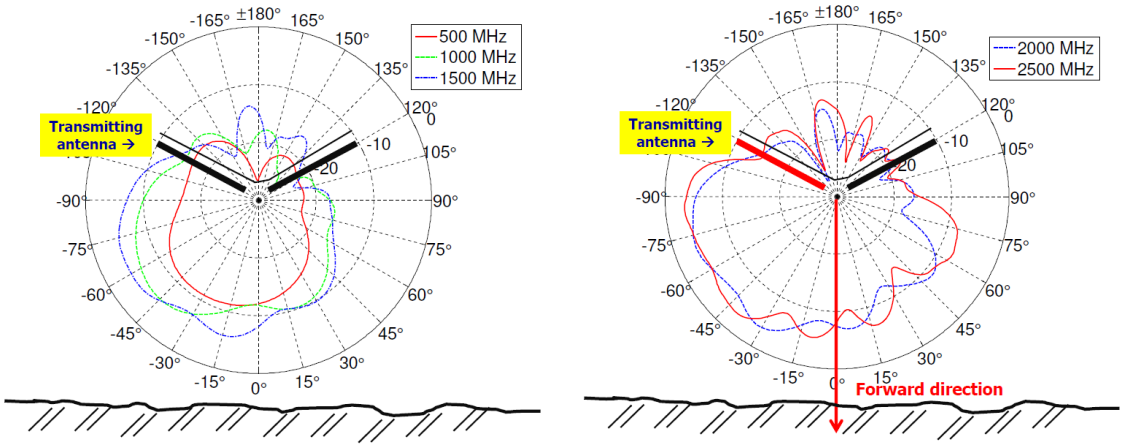

Figure 2-9. Simulated Radiation pattern of bowtie antenna (Eide and Sala 2012)

2.2.6 Application of 3-D GPR

It is known that EM waves can be reflected from local scatterers such as aggregate and air voids in asphalt pavement. Depending on the electrical size (size in terms of EM wave length) of the scatter, the EM scattering phenomenon can be different: if the scatterers are electrically small, the scattering effect is Rayleigh scattering; if the size of the scatterers are comparable to the EM wavelength, the scattering effect is in Mie scattering domain (Chuang 2009). For example, for a 2GHz horn antenna which is widely used in pavement surveys, the EM wavelength in free space is around 0.016m and the scattering effect in asphalt pavement is more significant than low frequency EM waves. At the same time, a high frequency antenna usually has a shorter pulse length in the time domain, which gives better time domain resolution. Therefore, there is a tradeoff between the penetration depth and the resolution: high frequency waves have shallow penetration depths and better resolution at the near surface area, while low frequency wavelengths are much

larger than the scale of pavement scatterer, allowing them to penetrate deeper into the ground but with lower resolution.

This is not a problem when the GPR survey is concentrated near the surface, such as in asphalt pavement surveys; however, if a complete survey is undertaken through the depths ranging from the surface to several meters deep, the use of a single frequency antenna can be problematic for the aforementioned reasons. Figure 2-10 shows the power received by a GPR antenna versus frequency at different depths. The dotted line represents the GPR sensitivity line, below which the EM signal power is too low for the receiver to sense. It is shown that at depth of 0.2m, signals at all frequencies can get strong reflected power. As the depth increases, only the low frequency portion of the spectrum is above the GPR sensitivity. This is consistent with the conclusion that the GPR is sensitive to each frequency only above a particular depth. Therefore, in order to obtain the most accurate data at each depth, one should eliminate the high frequency component in the spectrum that would otherwise produce only noise at large depths. In light of this, the ultra-wide band 3-D radar can be employed to generate 2D profiles at different depths.

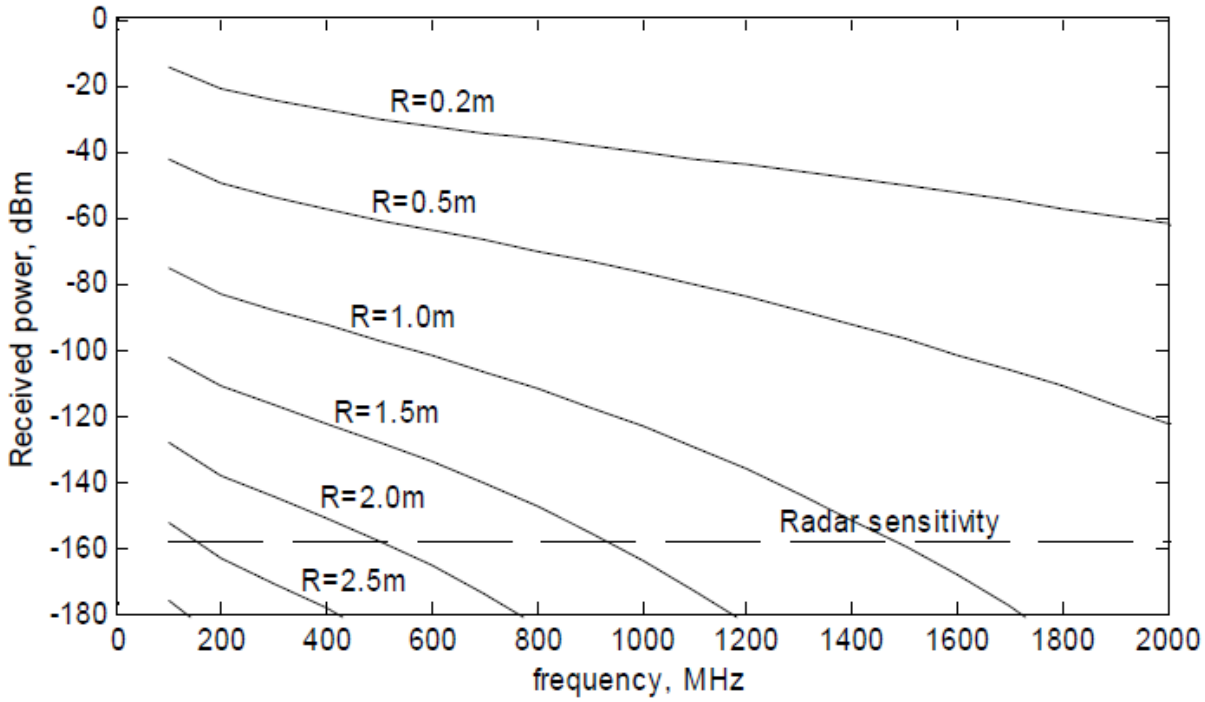

Figure 2-10. Received power spectrum at different depths (Eide and Jens 2002)

3-D GPR has been used for evaluating civil engineering structures over the past ten years. In 2001, 3-D GPR was successfully used in mapping pipes, cables, and old tramlines under streets in Trondheim, Norway (Eide and Jens 2002). During the survey, the 3-D radar was operated in the frequency range of 100MHz to 1.6GHz. The results of the study show that by applying different bandpass filters based on antenna sensitivity, utility lines under the pavement can be successfully mapped by 3-D GPR at different depths.

Another study compares the results of air-coupled 3-D GPR with 400 MHz ground-coupled pulsed antenna to detect underground archeological structures in the Roman town of Augusta Raurica, in Switzerland (Leckebusch 2011). The study concludes that the air-coupled 3-D GPR can penetrate less deeply as compared to the ground-coupled pulsed GPR, due to the high reflection at the ground-air interface of the air-coupled antenna.

2.3 GPR applications on asphalt pavement

2.3.1 Layer thickness estimation

The most prevalent application of GPR on asphalt pavement is the estimation of layer thickness, due to the straightforwardness of the surface reflection and the two-way travel time method. Many studies have examined using GPR for this application. Using the two-way travel time method, Al-Qadi *et al.* (2003) reported a mean thickness error of 2.9% for asphalt pavement layers ranging between 100 mm and 250 mm in thickness on a newly built test section of Route 288 in Richmond, Virginia, United States. Lahouar *et al.* (2002) analyzed GPR data collected from interstate highway I-81 using a kind of multi-offset measurement method – the common midpoint method (CMP) –reporting a thickness error ranging from 1% to 15% with a mean error of 6.8%. Liu *et al.* (2014) applied a similar CMP method and envelope velocity spectrum analysis to GPR data to measure the dielectric permittivity and thickness of snow and ice cover on a brackish lagoon, with good accuracy. Liu and Sato (2014) used another multi-offset measurement method – the common source method – for asphalt layer thickness and EM wave velocity estimation. In the study they first designed a Vivaldi antenna array and then calibrated the phase center using a gypsum model. The results from their field experiment shows that the error of asphalt layer thickness estimation is less than 6mm (10%). The Wide Angle Refraction and Reflection (WARR) method can also be used to measure the EM wave velocity within the surface layer and therefore the dielectric constant and thickness of the surface layer (Huisman *et al.* 2001).

2.3.2 Asphalt pavement density estimation

Asphalt pavement density is another important factor that influences the performance and service life of the pavement (Roberts et al. 1996). There have been many studies trying to predict

asphalt density from GPR survey data. Most of these methods attempted to correlate the dielectric constant of the asphalt concrete to the volumetric properties of asphalt pavement.

Currently there are two major methods for estimating asphalt pavement density from GPR data. The first method is to relate the asphalt pavement density to its dielectric constant using an empirical regression model (Saarenketo and Scullion 2000; Kassem et al. 2012; Saarenketo 1997). The second method is to use density models between the bulk specific gravity and dielectric constant of asphalt mixture according to the EM mixing theory (Al-Qadi et al. 2010; Leng et al. 2011; Leng et al. 2012; Shangguan et al. 2014a).

2.4 Summary

Predicting asphalt pavement layer thicknesses accurately helps to evaluate the pavement condition. Current coring methods, used to estimate the asphalt layer thicknesses, have limitations. GPR represents an alternative non-destructive approach. The XCMP method overcomes the disadvantage of the traditional surface reflection methods. The recent developed 3-D GPR is a multi-channel antenna array, and can therefore collect data at a relatively high speed. The combination of XCMP method and 3-D GPR will allow rapid data collection speed while maintain an accurate layer thickness prediction. This reflects the main objective of the thesis. Detailed research approach follows.

CHAPTER 3: RESEARCH APPROACH

3.1 Extended CMP method

Multi-offset methods were originally used in seismic migration to measure seismic wave velocity (Yilmaz 2008). The common source method and common midpoint (CMP) method are the two common multi-offset techniques (Schneider 1984). The CMP method has been recently used to calculate the EM wave velocity within asphalt concrete pavement layers (Lahouar 2002).

Figure 3-1 shows a simple CMP configuration to measure the surface layer thickness with a monostatic ground-coupled GPR system and a bistatic ground-coupled GPR system. In Figure 2-11, "Tx" and "Rx" represent the transmitting and receiving antenna, respectively. The antennas are placed on the surface of an asphalt concrete pavement of thickness "h" at distance x/2 from each other. As a result of the geometry configuration, the reflection location of the bistatic system and monostatic system at the bottom of the surface layer should be the same point P.

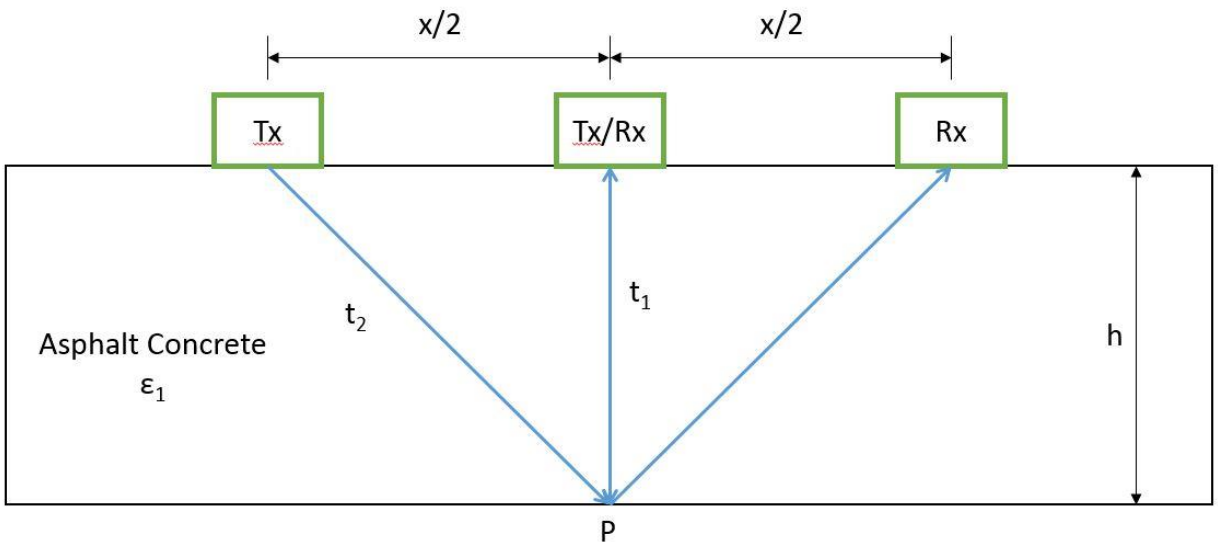

Figure 3-1. CMP configuration using ground-coupled GPR system

From Figure 2-11 we can write the following equations:

$$vt_1 = 2h \tag{3-1}$$

$$vt_2 = 2\sqrt{h^2 + \left(\frac{x}{2}\right)^2} \tag{3-2}$$

where t_1 is the two way-travel time from point P of the monostatic system and t_2 is the two-way travel time from point P of the bistatic system. From Equations (3-1) and (3-2), the layer thickness h and EM wave velocity can be calculated:

$$v = \frac{x}{\sqrt{t_2^2 - t_1^2}} \tag{3-3}$$

$$h = \frac{2xt_1}{\sqrt{t_2^2 - t_1^2}} \tag{3-4}$$

The dielectric constant of the asphalt concrete can then be obtained from $v = \frac{c}{\sqrt{\varepsilon_1}}$.

Therefore, once the two-way travel times of both antenna systems are obtained from the collected signals, the dielectric constant as well as the layer thickness can be obtained. This assumes that the pavement is thick enough, or the frequency band of the EM wave is wide enough, and that the two pulses reflected from the surface and the bottom of the layer can be distinguished—i.e., there is enough time resolution. Otherwise, super resolution techniques such as deconvolution need to be used to distinguish the overlapping pulses (Zhao et al. 2015; La Bastard et al. 2012).

In the previous discussed CMP method, we assume that the two antenna systems are all ground-coupled systems. However, in this study, the available 3-D GPR is an air-coupled system. One of the advantages of an air-coupled system is that it doesn't require direct contact with the

ground surface, allowing it to collect data continuously and at high speeds (Shangguan and Al-Qadi 2014). Leng and Al-Qadi (2014) developed an extended CMP (XCMP) method that can be applied to two air-coupled bistatic antenna systems. Details on XCMP algorithm by Leng and Al-Qadi (2014) is presented herein for the completeness of the study.

Figure 3-2 shows the configuration of the XCMP method. Two air-coupled bistatic antenna systems are used. As in Figure 3-1, "Tx" and "Rx" represent the transmitting and receiving antenna, respectively. In Figure 3-2, the antenna height is d; the pavement thickness is h; the distance between antenna pairs Tx_1/Rx_1 and Tx_1/Rx_2 is x_{01} and x_{02}, respectively, and they share the same midpoint P_1 and P_2. The dielectric constant of the free space (air) and the asphalt concrete is $\varepsilon_0 = 1$ and ε_1, respectively. Figure 3-2(a) shows the reflection paths from surface of the asphalt concrete layer, where the two-way travel times of antenna pairs Tx_1/Rx_1 and Tx_1/Rx_2 are t_{11} and t_{21}, respectively. Figure 3-2(b) shows the reflection path from bottom of the layer, where the two-way travel times of antenna pairs Tx_1/Rx_1 and Tx_1/Rx_2 in the air are t_{12} and t_{22}, respectively; the two-way travel times of antenna pairs Tx_1/Rx_1 and Tx_1/Rx_2 in the pavement are t_1 and t_2, respectively; the incident angles at the surface of the layer of antenna pairs Tx_1/Rx_1 and Tx_1/Rx_2 are θ_{i1} and θ_{i2}, respectively; and the transmission angles at the surface of the layer of antenna pairs Tx_1/Rx_1 and Tx_1/Rx_2 are θ_{t1} and θ_{t2}, respectively.

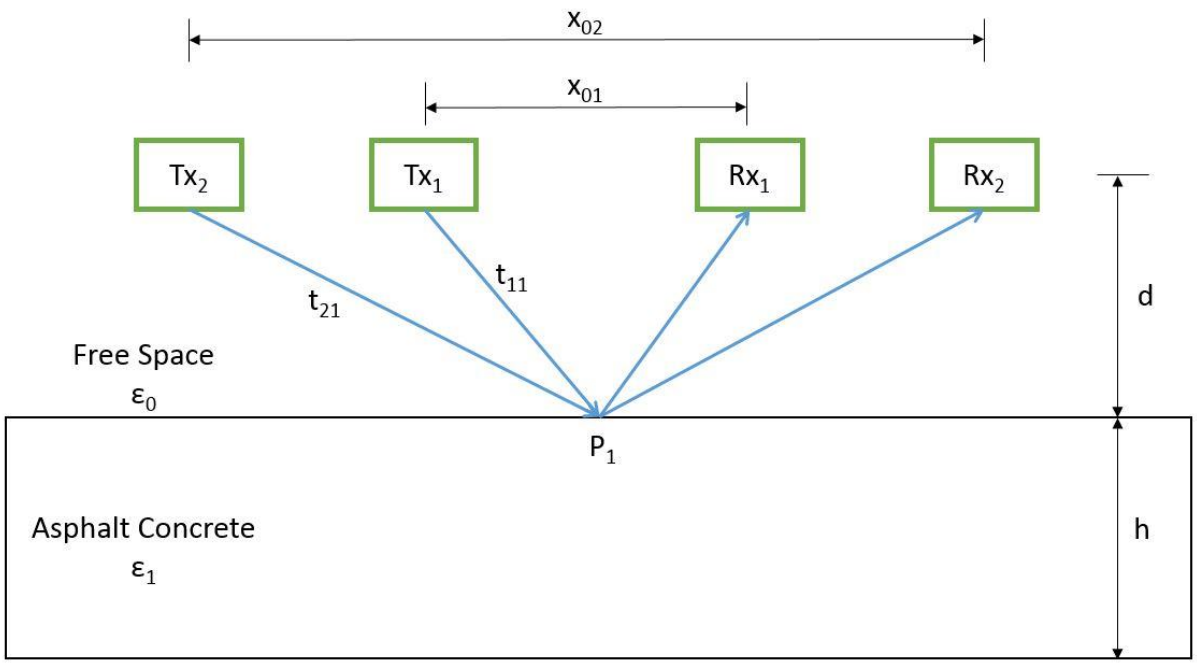

(a)

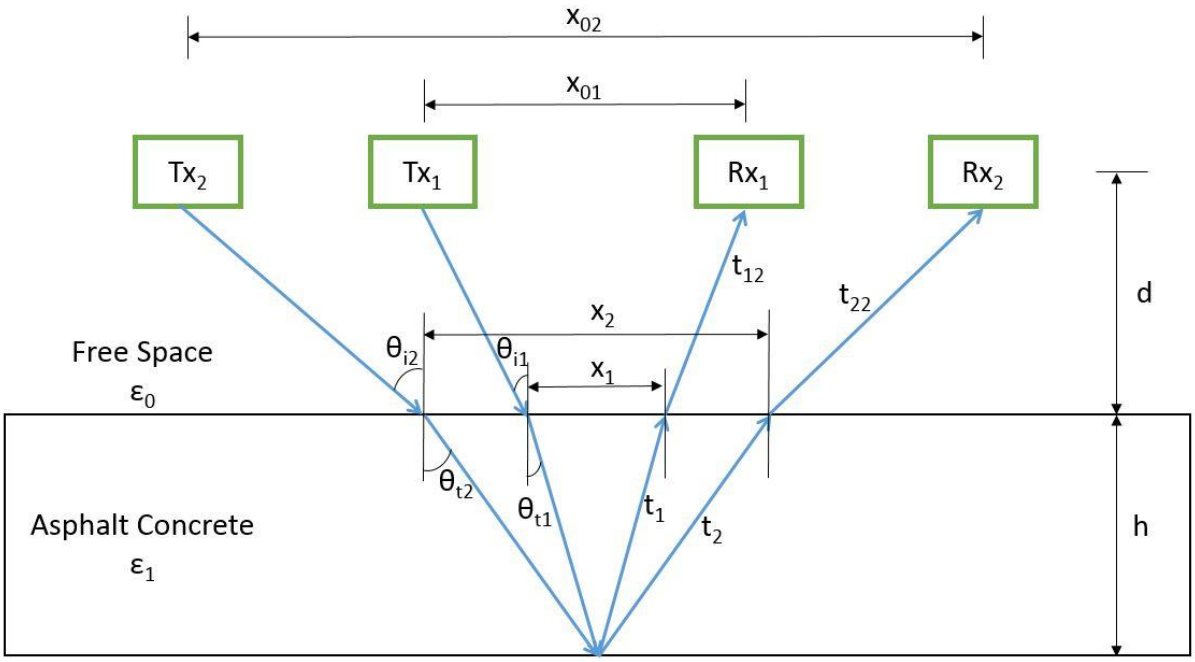

(b)

Figure 3-2. XCMP configuration with two are-coupled bistatic antenna system: (a) reflection from surface of the layer; (b) reflection from bottom of the layer

According to Snell's law of transmission, the incident angle and transmission angle in Figure 3-2(b) has the following relationship (Jin 2011):

$$\frac{\sin\theta_{i1}}{\sin\theta_{t1}} = \frac{\sin\theta_{i2}}{\sin\theta_{t2}} = \sqrt{\varepsilon_1} \tag{3-5}$$

The following equations can be derived based on the geometry information in Figure 3-2:

$$vt_1 = 2\sqrt{h^2 + \left(\frac{x_1}{2}\right)^2} \tag{3-6}$$

$$vt_2 = 2\sqrt{h^2 + \left(\frac{x_2}{2}\right)^2} \tag{3-7}$$

$$\sin\theta_{t1} = \frac{x_1/2}{vt_1/2} = \frac{x_1\sqrt{\varepsilon_1}}{ct_1} \tag{3-8}$$

$$\sin\theta_{t2} = \frac{x_2/2}{vt_2/2} = \frac{x_2\sqrt{\varepsilon_1}}{ct_2} \tag{3-9}$$

$$\tan\theta_{i1} = \frac{x_{01} - x_1}{2d} \tag{3-10}$$

$$\tan\theta_{i2} = \frac{x_{02} - x_2}{2d} \tag{3-11}$$

where $v = \frac{c}{\sqrt{\varepsilon_1}}$ is the EM wave velocity in the asphalt concrete.

Combining Equations (3-6) and (3-7) and plugging in $v = \frac{c}{\sqrt{\varepsilon_1}}$ yields:

$$\varepsilon_1 = \frac{c^2(t_2^2 - t_1^2)}{x_2^2 - x_1^2} \tag{3-12}$$

Combining Equations (3-5) and (3-8) with (3-12), the following two equations can be obtained:

$$\left(\frac{x_{01} - x_1}{2d}\right)^2 + 1 = \frac{t_1^2(x_2^2 - x_1^2)^2}{t_1^2(x_2^2 - x_1^2)^2 - x_1^2 c^2(t_2^2 - t_1^2)^2} \tag{3-13}$$

$$\left(\frac{x_{02} - x_2}{2d}\right)^2 + 1 = \frac{t_2^2(x_2^2 - x_1^2)^2}{t_2^2(x_2^2 - x_1^2)^2 - x_2^2 c^2(t_2^2 - t_1^2)^2} \tag{3-14}$$

There are four unknowns in Equations (3-13) and (3-14): x_1, x_2, t_1, and t_2. In order to solve these four unknowns, two additional equations are required. It should be noted that the information from the collected GPR signals has not been used. Figure 3-3 is an example of the collected GPR signals from two air-coupled 3-D GPR antenna pairs. Since the 3-D GPR collects data in the frequency domain, this figure shows the time domain amplitude data after inverse Fourier Transform and the data are therefore all positive. In Figure 3-3, both Tx/Rx pairs have receive three significant pulses: the first one is the direct coupling pulse, the second one is the reflection from the surface of the pavement, and the third one is the reflection from the bottom of the pavement layer.

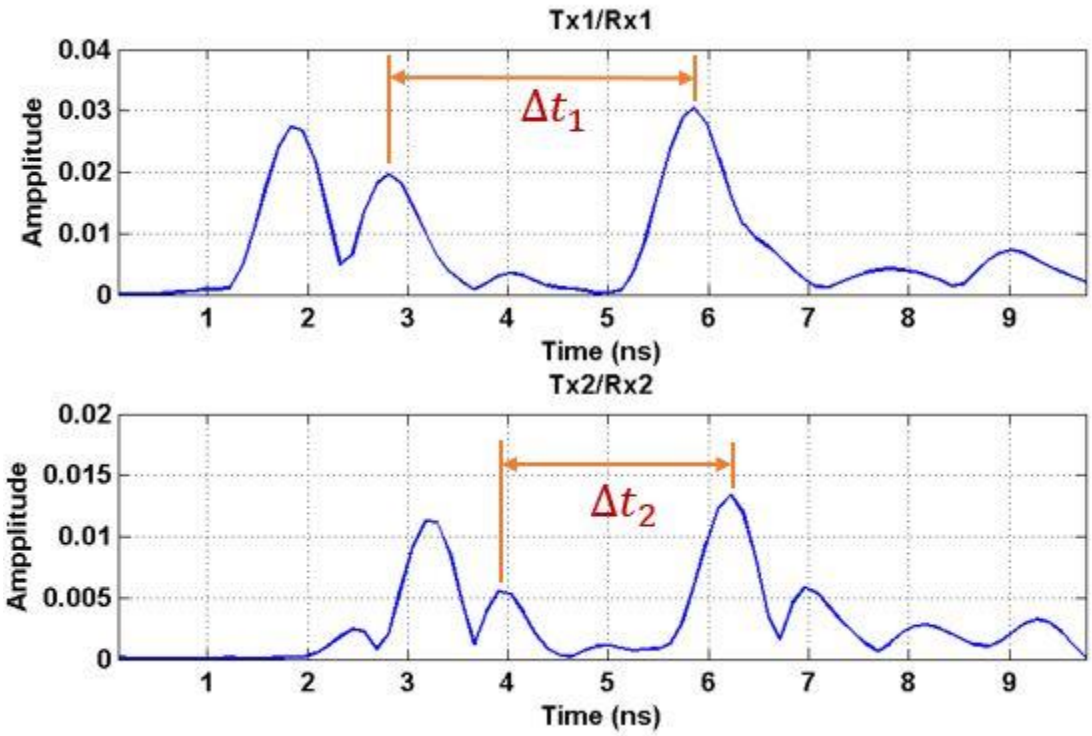

Figure 3-3. Collected XCMP GPR signals from two air-coupled 3-D GPR antenna pairs

As shown in Figure 3-3, the time difference between the surface reflection and the reflection at the bottom of the layer Δt_1 and Δt_2 can be directly obtained from the collected data, and they can be expressed as follows:

$$\Delta t_1 = t_{12} + t_1 - t_{11} \tag{3-15}$$

$$\Delta t_2 = t_{22} + t_2 - t_{21} \tag{3-16}$$

where

$$t_{11} = \frac{2\sqrt{d^2 + x_{01}^2 / 4}}{c} \tag{3-17}$$

$$t_{21} = \frac{2\sqrt{d^2 + x_{02}^2 / 4}}{c} \tag{3-18}$$

$$t_{12} = \frac{2\sqrt{d^2 + (x_{01} - x_1)^2 / 4}}{c} \tag{3-19}$$

$$t_{22} = \frac{2\sqrt{d^2 + (x_{02} - x_2)^2 / 4}}{c} \tag{3-20}$$

Therefore, the following two equations can be obtained by substituting Equations (3-17) to (3-20) into Equations (3-15) and (3-16):

$$\Delta t_1 = t_1 + \frac{2\sqrt{d^2 + (x_{01} - x_1)^2 / 4}}{c} - \frac{2\sqrt{d^2 + x_{01}^2 / 4}}{c} \tag{3-21}$$

$$\Delta t_2 = t_2 + \frac{2\sqrt{d^2 + (x_{02} - x_2)^2 / 4}}{c} - \frac{2\sqrt{d^2 + x_{02}^2 / 4}}{c} \tag{3-22}$$

With Equations (3-13), (3-14), (3-21) and (3-22), the four unknowns x_1, x_2, t_1, and t_2 can be solved numerically using the optimization method described in Section 3.3.3. The dielectric constant of asphalt concrete ε_1 and the asphalt layer thickness h can then be obtained from Equations (3-12) and (3-6), respectively.

3.2 Experiment plan with 3-D GPR to validate XCMP method

With the XCMP method described in the previous section, Leng and Al-Qadi (2014) successfully validated that the pulsed antenna can provide better accuracy in determining asphalt pavement layer thickness than the surface reflection method. In that study, two air-coupled horn antennas manufactured by Geophysical Survey Systems, Inc. (GSSI) were used (Figure 2-1). A test site was constructed as shown in Figure 3-4.

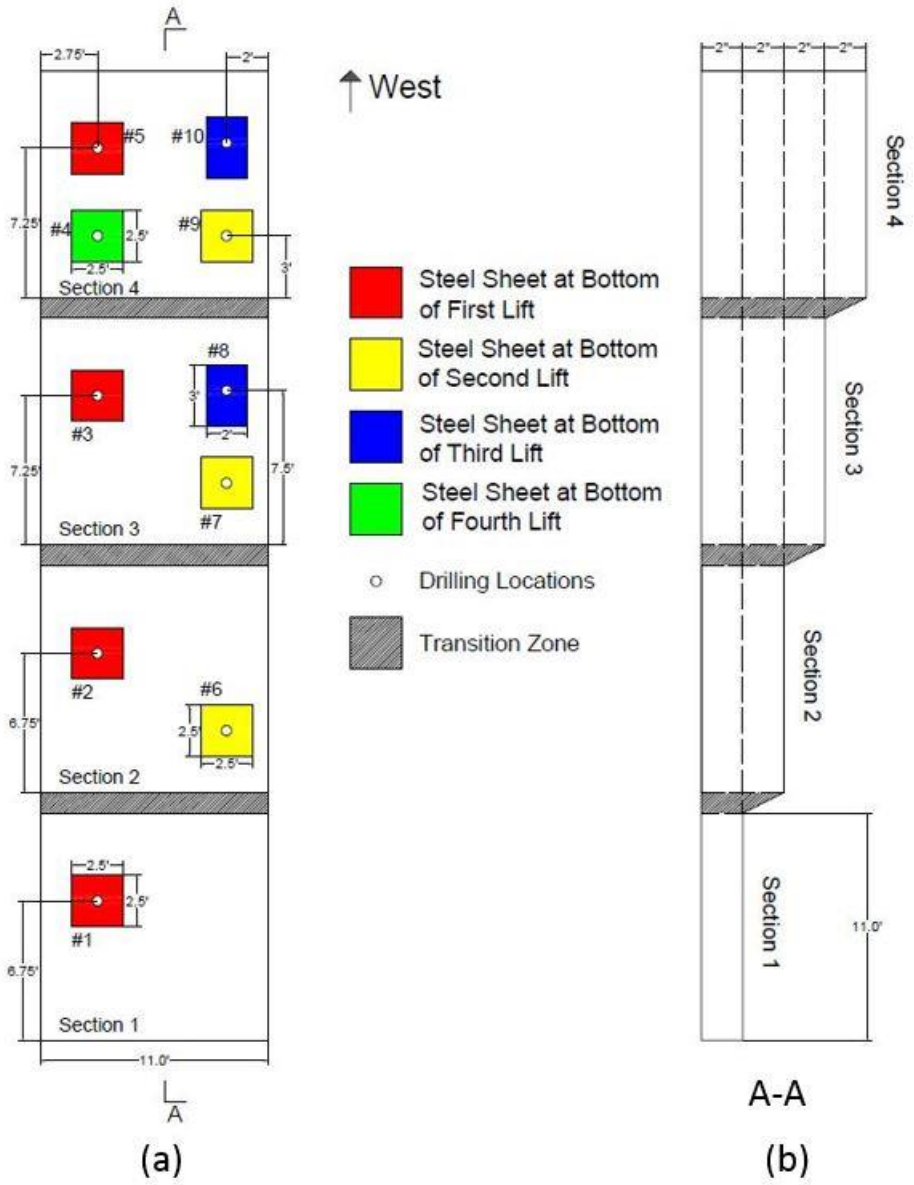

Figure 3-4. Test site configuration plan: (a) top view; (b) side view

The test site has four sections, each of which is a 3.35m by 3.35m (11 ft by 11 ft) square. The design thicknesses of sections one to four are 50.8mm, 101.6mm, 152.4mm, and 203.2mm (2 in, 4 in, 6 in, and 8 in), respectively. There are three transition zones between each section to facilitate the construction process. Each transition zone has a length of 3.96m (13 ft) and is left incomplete, as shown on Figure 3-4, for simplicity.

There are steel plates placed at the bottom of each asphalt lift to increase the reflection coefficient at the bottom of the pavement, since it can then be regarded as a perfect reflector, reflecting back all the EM wave energy. This is not necessary in practice when the dielectric constant difference between the surface layer and the bottom layer is significant. The layout of the steel plates is shown in Figure 3-4: section n has n steel plates embedded in the asphalt concrete at different depths, where n=1 to 4.

This study used a DX1821 antenna array manufactured by 3D-Radar Company. Similar to the one shown in Figure 2-7, the DX1821 system has a total of eleven bow-tie monopole transiting antennas and eleven bow-tie monopole receiving antennas. It has a total length of 1.8m with an effective scan width of 1.575m. Each of the bow-tie antenna has an ultra-wide frequency band from 200MHz to 3GHz and can radiate EM signal in a stepped frequency manner, as explained in section 2.1.3. The antenna spacing is 0.15m. A total of 21 channels could be configured arbitrarily between one transmitting antenna and one receiving antenna (3D-Radar GPR 2015).

To survey the whole lane, a wood trailer was built to carry the antenna array—as shown in Figure 3-5—together with the antenna array and control unit. After calibration, the phase center of each bow-tie antenna was found to be 0.369m above the ground.

In order to apply the XCMP method, several different antenna scan patterns are designed to have multiple XCMP offsets. The authors devised total five testing plans to find the best configuration based on the results. Plan 1 is XCMP 1-3, meaning that the cross-line offset between Tx1/Rx1 is 1 intervals, and the cross-line offset between Tx2/Rx2 is 3 intervals. “In-line” and “cross-line” refer to the directions parallel to the survey direction and the length of the antenna array, respectively, and the cross-line intervals and in-line intervals were 0.075m and 0.44m, respectively, as shown in Figure 3-6. Similarly, Plan 2 is XCMP 1-5, Plan 3 is XCMP 1-7, Plan 4

is XCMP 3-5, and Plan 5 is the standard scan pattern, meaning that each of the Tx/Rx pairs has an in-line offset of 1 spacing. Table 3-1 shows all the testing plans. It should be noted that the distances in Table 3-1 are the actual distances. Figure 3-6 illustrates plan 2: XCMP 1-5 configuration. As shown in Figure 3-6, the standard scan pattern has 21 measuring points (denoted by the yellow circle at the center point of each antenna pair). Using all 21 channels, by changing the antenna Tx/Rx match, we can set up the XCMP 1-5 configuration as shown in the blue lines in Figure 3-6. The trade-off is that only 9 points can be surveyed in the XCMP 1-5 method as compared with 21 points in the standard survey plan. Since the DX 1821 antenna array is about half the width of the survey lane, two GPR surveys were conducted to cover the whole length: one along the center of the south side of the survey lane, and the other along the center of the north side of the survey lane.

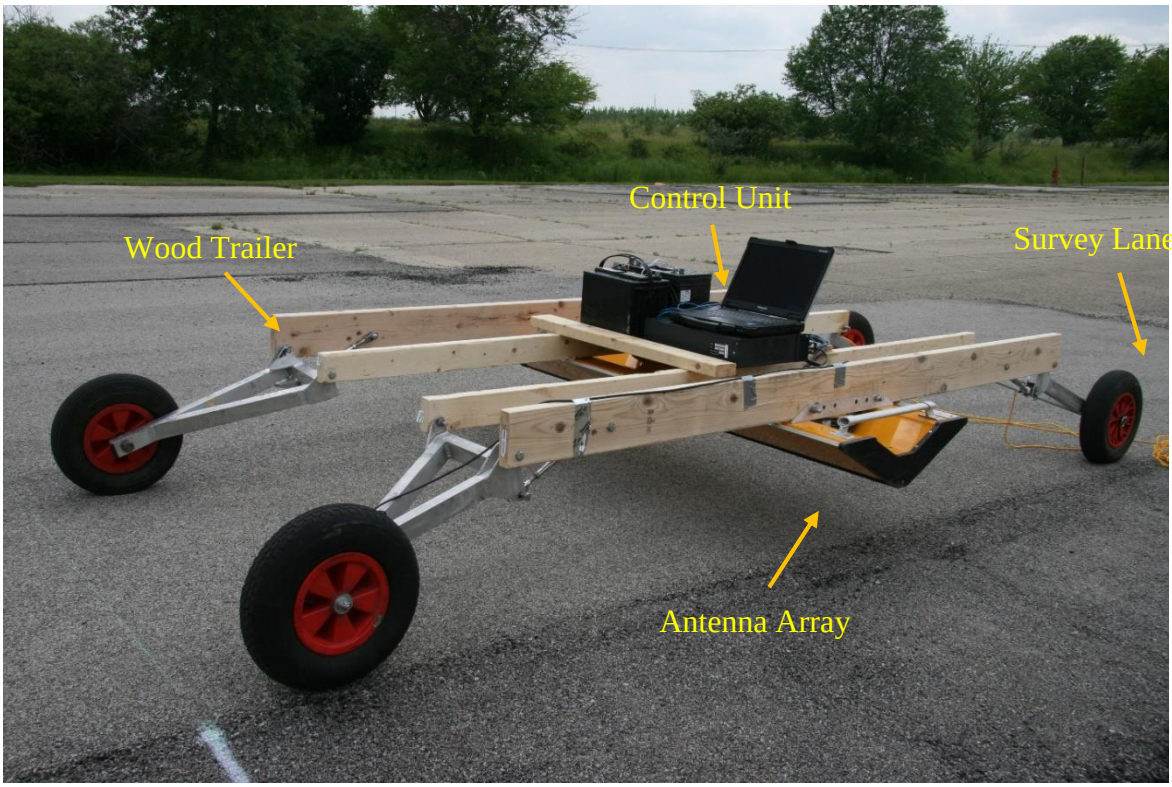

Figure 3-5. DX1821 antenna array and wood trailer

Table 3-1. XCMP antenna setting plans

Plan	1	2	3	4	5
Configuration	XCMP 1-3	XCMP 1-5	XCMP 1-7	XCMP 3-5	Standard
Distance between Tx/Rx pair 1 (m)	0.446	0.446	0.446	0.369	0.446
Distance between Tx/Rx pair 2 (m)	0.369	0.578	0.685	0.578	-

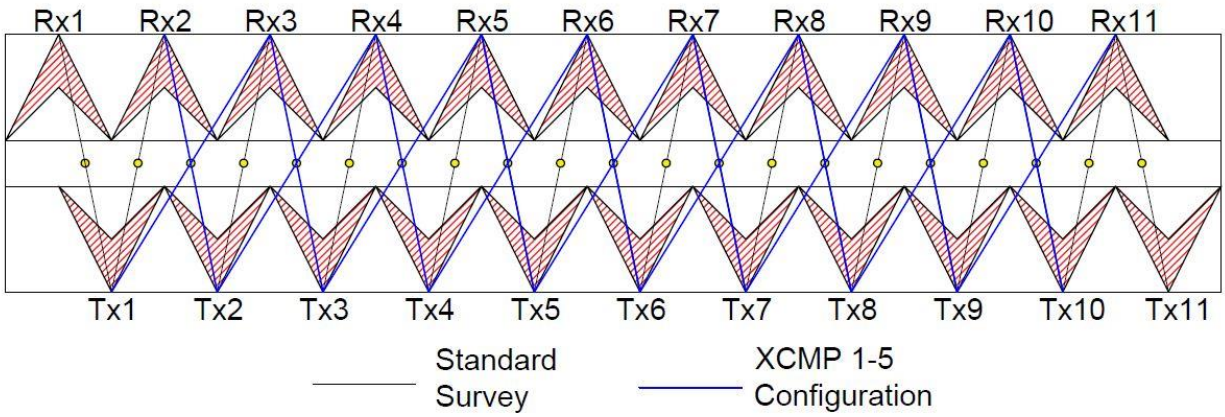

Figure 3-6 DX 1821 antenna array layout, standard survey and XCMP 1-5 test configuration

After all 10 GPR surveys (2 surveys for each test plan) were completed, the collected GPR data were converted to time domain signals and corresponding signal processing techniques were applied (see Section 3.3). The signal directed reflected from the center of each steel plate was used to calculate the dielectric constant and layer thickness. The signal reflected from the center of each steel plate can be approximated found by identifying the maximum reflection amplitude.

Cores were drilled at the center of each steel plate and their thicknesses were measured in the laboratory to provide the as-built pavement thicknesses of each section. The accuracy of the proposed algorithm could then be evaluated (see Section 4).

3.3 Signal Processing

3.3.1 3-D GPR signal characteristics

As explained in section 2.1.2, the resolution of a signal is important as it determines the ability to distinguish adjacent pulses. Where GPR is used to determine asphalt layer thickness by applying a two-way travel method, the time domain resolution of the GPR signal is critical, due to the reasons explained in section 3.1. When the XCMP method is used, it is also necessary to distinguish the reflection from the surface and the bottom of the surface layer to obtain Δt_1 and Δt_2 in Equations (3-15) and (3-16). An example of the 3-D GPR signal reflected back from a two-layered asphalt pavement system is shown in Figure 3-7. The Rayleigh resolution of the signal was found to be 0.61ns, as shown in Figure 3-7. Therefore, if the 3-D GPR signal is normally incident on the pavement whose dielectric is 4, the smallest thickness that can be resolved is $0.61ns \times 3 \times 10^8 / \sqrt{6} m/s = 74.7mm$, which about 75mm. For a GSSI 2GHz horn antenna, the Rayleigh resolution is 0.5382ns. This shows that the pulsed horn antenna has good time domain resolution due to its wide bandwidth.

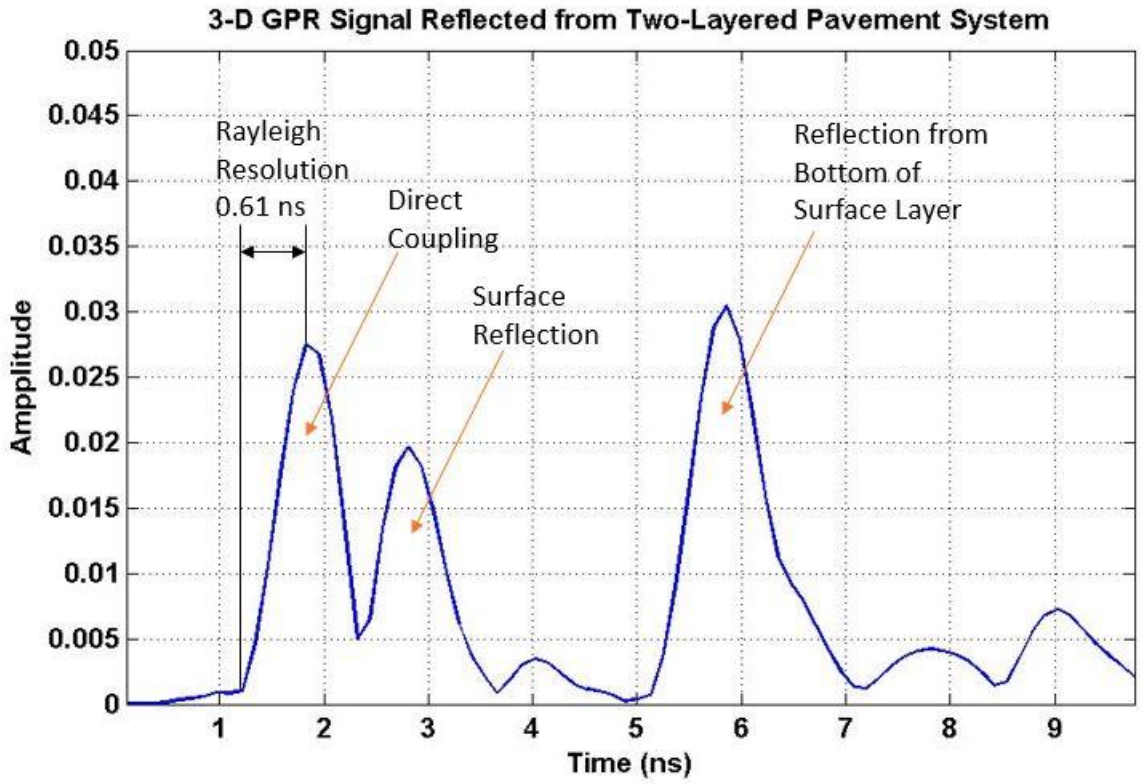

Figure 3-7. 3-D GPR signal over a two-layered asphalt pavement system

3.3.2 Whittaker–Shannon interpolation

According to section 3.1, the result of XCMP problem can be obtained by solving a set of four non-linear equations (3-13), (3-14), (3-21) and (3-22). Numerical solutions, such as least square solutions, are needed to solve these equations. However, such equations are not necessarily stable, meaning that a small disturbance in the inputs (x_{01}, x_{02}, d, Δt_1 and Δt_2) could have a huge influence on the outputs (x_1, x_2, t_1, and t_2). The layout of the 3-D GPR was provided by the 3-D Radar Company and therefore the values of x_{01}, x_{02} and d have been well calibrated to yield sufficient accuracy. After sensitivity analysis, we also found that the output results are most sensible to the change of Δt_1 and Δt_2.

Since the 3-D GPR collects signal in the frequency domain, the time domain signal is "synthetized" by inverse Fourier transform of the frequency domain signal, and the time domain signal sampling interval is directly related to the frequency bandwidth, according to the Discrete Fourier Transform (DFT) property:

$$dt = \frac{1}{f} \tag{3-23}$$

where dt is the time domain sampling interval and f is the upper limit of the frequency band. For the DX1821 3-D GPR, the time domain sampling interval is 0.12207 ns, and the corresponding upper limit of the frequency band is 8.19 GHz. Compared with the time domain sampling interval of a 2 GHz GSSI pulsed horn antenna—which is 0.0234ns according to Zhao et al. (2015)—it is shown that the 3-D GPR has a smaller time domain sampling interval. In other words, the frequency band of 3-D GPR is not significantly wider than that of the 2 GHz GSSI pulsed horn antenna. However, if we assume that the frequency content of the 3-D GPR signal above the upper limit of the frequency band is all zero, then the time domain sampling interval of the signal can be decreased by zero padding the frequency domain signal (Lyons 2010). The corresponding time domain process is the Whittaker–Shannon interpolation, or the Sinc interpolation:

$$x(t) = \sum_{n=-\infty}^{\infty} x[n]\mathrm{sinc}\left(\frac{t - ndt}{dt}\right) \tag{3-24}$$

where discrete time signal $x[n]$ is continuous time signal $x(t)$ sampled at ndt, n is an integer, $\mathrm{sinc(x)} = \frac{\sin(x)}{x}$ is the sinc function, and dt is the time domain sampling interval. If the sampling interval dt meets the Nyquist criteria—i.e. the sampling frequency 1/dt is higher than twice the maximum frequency content of the analog signal—then Equation (3-24) can perfectly restore the

original analog signal $x(t)$; otherwise Equation (3-24) gives an approximation of the original analog signal $x(t)$. In practice, we can again sample $x(t)$ with a finer sampling interval to obtain the time domain signal with desired time sampling interval:

$$x_{new}[m] = x(mT) = \sum_{n=-\infty}^{\infty} x[n]\mathrm{sinc}\left(\frac{mT - ndt}{dt}\right) \tag{3-25}$$

where $x_{new}[m]$ is the interpolated discrete signal, m is an integer, and T is the desired time domain sampling interval. From a signal processing point of view, Equation (1.1) can be considered as, first, up-sampling the discrete signal x[n] and then, second, filtering the up-sampled signal $x_{new}[m]$ with an ideal low pass filter. The process can also be performed in the frequency, and the corresponding technique called the frequency zero padding; i.e., if we want to perform a k point sinc interpolation on x[n], we can first pad zeros behind $X(\omega)$, the DFT of x[n], such that the length of the padded frequency series is m times longer than the original $X(\omega)$, and then do the inverse DFT on the zero padded frequency series. In this study, it was found that a one-hundred point Whittaker–Shannon interpolation could provide a sufficient time domain sampling interval.

3.3.3 Numerical solving technique

After Δt_1 and Δt_2 are obtained from the interpolated signals, based on Equations (3-13), (3-14), (3-21) and (3-22), the four unknowns x_1, x_2, t_1, and t_2 can be solved. Since Equations (3-13) and (3-14) cannot be solved analytically, the least square solutions of x_1 and x_2 are calculated. The entire solving process is summarized below.

1) Select the GPR signals reflected from each steel plate (the maximum reflection coefficient location).

2) Perform 100-points Whittaker–Shannon interpolation on each of the GPR signals.

3) From Equations (3-21) and (3-22), t_1 and t_2 can be expressed in terms of x_1 , x_2 . Substituting t_1 and t_2 into Equations (3-13) and (3-14) yields two equations with two unknowns x_1 and x_2 .

4) Discretize x_1 and x_2 with distance step of 0.001 m in the range $x_1 \in (0, x_{01}), x_2 \in (x_1, x_{02})$ according to Figure 3-2(b).

5) Find the x_1 and x_2 , such that the residue of the Equations (3-13) and (3-14) are minimized:

$$[x_1, x_2] = \underset{x_1 \in (0, x_{01}), x_2 \in (x_1, x_{02})}{\arg\min} \left(norm([r_1, r_2]) \right) \tag{3-26}$$

where r_1 and r_2 are the residues of Equations (3-13) and (3-14), respectively. It should be noted that if the minimum norm is located at the boundary of the area $x_1 \in (0, x_{01}), x_2 \in (x_1, x_{02})$, the resulting x_1 and x_2 are not the solutions of Equations (3-13) and (3-14).

6) Find t_1 and t_2 From Equations (3-21) and (3-22).

7) Find the dielectric constant of the asphalt concrete ε_1 from Equation (3-12).

8) Find the layer thickness *h* from Equation (3-6) or (3-7).

CHAPTER 4: TEST RESULTS AND DISCUSSION

4.1 3-D GPR standard scan pattern results

Before doing the XCMP test, a 3-D GPR survey with the standard scan pattern was first conducted to show the layout of the two asphalt pavement lanes. The trigger distance was set to 7.504183cm, the depth range set to 125ns, and the dwell time set to 1ns. The detailed scan pattern is shown in Table 4-1. “Tx” means the transmitting antenna and “Rx” means the receiving antenna as shown in Figure 3-6.

Table 4-1. Standard scan pattern

Channel	1	2	3	4	5	6	7	8	9	10	11	12	13	14	15	16	17	18	19	20	21
Tx	1	2	2	3	3	4	4	8	8	6	6	7	7	8	8	9	9	10	10	11	11
Rx	1	1	2	2	3	3	4	4	5	5	6	6	7	7	8	8	9	9	10	10	11

For each of the two lanes, the collected signal is a 245 by 409 by 21 three dimensional matrix, where 245 is the number of time steps, representing the through depth direction, 409 is the number of scans along the lane, representing the in-line direction, and 21 is the number of channels, representing the cross-line direction. By selecting different time steps, we can obtain the horizontal slices of the pavement at different depths. For example, Figures 4-1 and 4-3 show the four slices at the depths of the embedded steel plates for both south and north lanes.

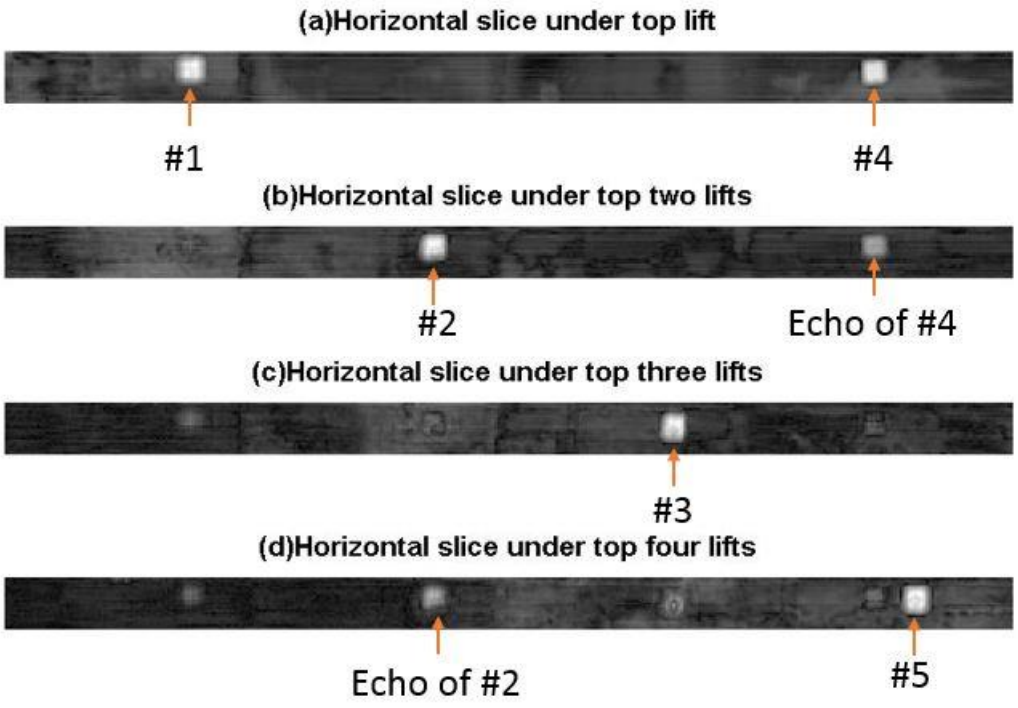

Figure 4-1. Horizontal slices at different depths for south lane

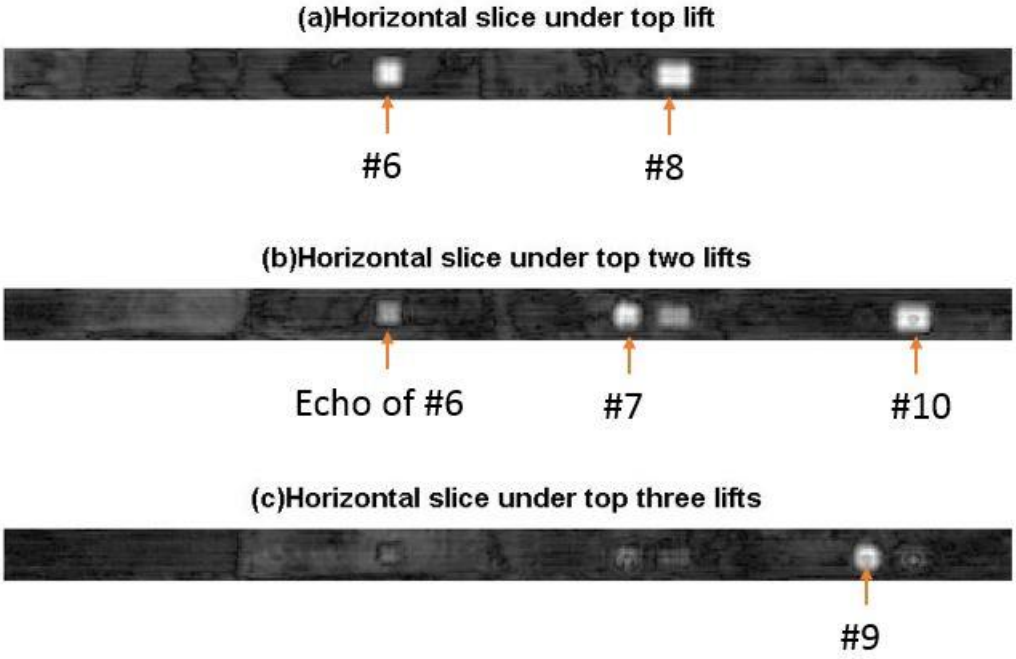

Figure 4-2. Horizontal slices at different depths for north lane

The rectangular spots in Figures 4-1 and 4-2 represent areas with very high reflection coefficients, corresponding to the places where steel plates are embedded. Together with the steel plate configuration shown in Figure 3-4, we can see that by selecting the GPR signals at different horizontal slices corresponding to the depth of the steel plate, the steel plates can be clearly seen. This shows the ability of 3-D GPR to map pavement sections accurately and rapidly. It should be noted that in some of the GPR horizontal slice signals, there are some rectangular spots resulting from the echoing effect, which is caused by the EM wave bouncing back and forth between asphalt layers. The echoing effect can be better observed in the vertical slices of the GPR data. Figures 4-3 and 4-4 are two vertical slices passing through the center of each steel plate in both south and north lanes. The "white line" at the top of both figures is the direct coupling pulse due to the antenna interaction, and the second "white line" is the reflection at the surface of the asphalt pavement. The short "white plateau" represents the location where steel plates are embedded. The echoing effect can be clearly seen beneath each of the steel plates.

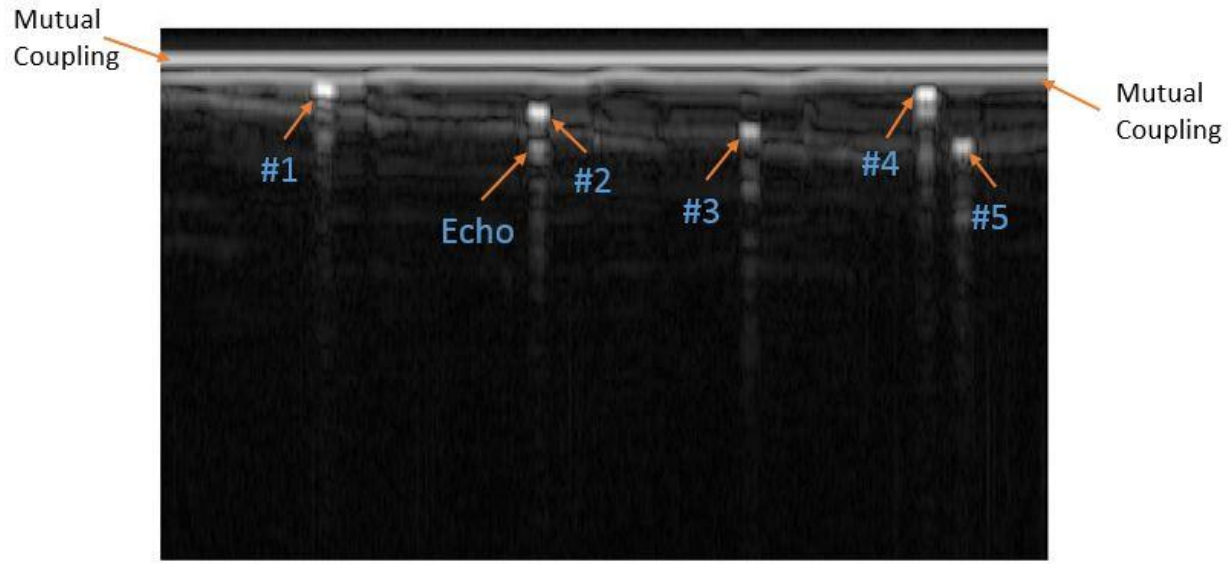

Figure 4-3. Vertical slice passing the center of each steel plates in south lane

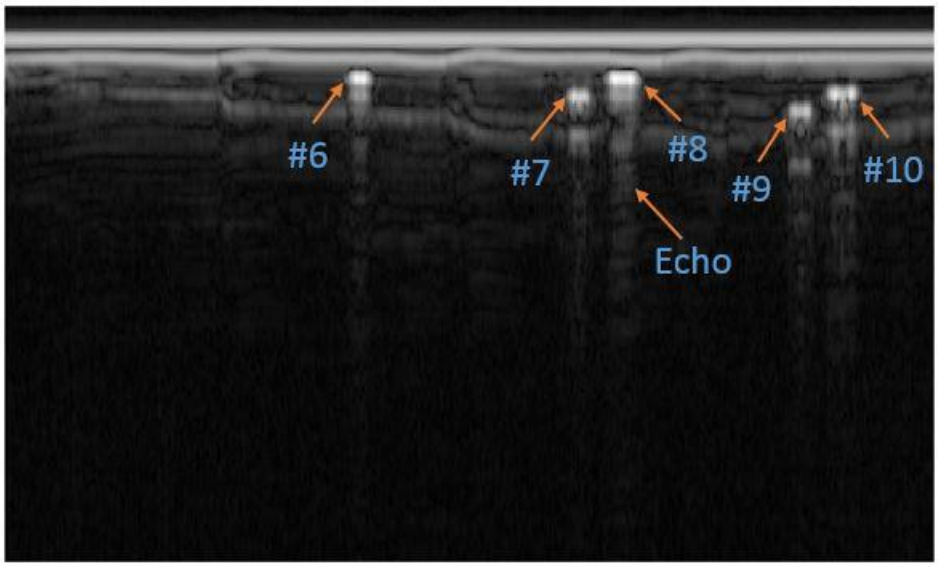

Figure 4-4. Vertical slice passing the center of each steel plates in north lane

Figures 4-3 and 4-4 are also called the "B-scan" GPR images. From the B-scan of the 3-D GPR, the steel plates can be clearly seen. The layer structure can also be seen, but not as clearly as the steel plates. This also shows that the two way travel time can be obtained directly from the GPR signal except for the case of steel plate #1, where the reflection overlaps with the surface reflection due to the layer thinness. Therefore, once an accurate dielectric constant is obtained, a depth map can be generated by converting the time based signals to depth based signals.

4.2 XCMP test results

Four XCMP testing plans were performed to obtain the depth of the steel plates; i.e., XCMP 1-3, XCMP 1-5, XCMP 1-7, and XCMP 3-5, as shown in Table 3-1. The detailed testing plan configurations are shown in Tables 4-2 to 4-5. All of the other parameters, including the trigger distance, the depth range, and the dwell time, were the same as the standard testing plan as explained in section 4.1.

Table 4-2. XCMP 1-3 scan pattern

Channel	1	2	3	4	5	6	7	8	9	10	11	12	13	14	15	16	17	18
Tx	2	3	3	4	4	5	5	6	6	7	7	8	8	9	9	10	10	11
Rx	2	1	3	2	4	3	5	4	6	5	7	6	8	7	9	8	10	9

Table 4-3. XCMP 1-5 scan pattern

Channel	1	2	3	4	5	6	7	8	9	10	11	12	13	14	15	16	17	18
Tx	2	1	3	2	4	3	5	4	6	5	7	6	8	7	9	8	10	9
Rx	2	3	3	4	4	5	5	6	6	7	7	8	8	9	9	10	10	11

Table 4-4. XCMP 1-7 scan pattern

Channel	1	2	3	4	5	6	7	8	9	10	11	12	13	14
Tx	3	5	4	6	5	7	6	8	7	9	8	10	9	11
Rx	3	1	4	2	5	3	6	4	7	5	8	6	9	7

Table 4-5. XCMP 3-5 scan pattern

Channel	1	2	3	4	5	6	7	8	9	10	11	12	13	14
Tx	5	3	6	4	7	5	8	6	9	7	10	8	11	9
Rx	3	5	4	6	5	7	6	8	7	9	8	10	9	11

After all GPR data are collected, the one hundred point Whittaker–Shannon interpolation was performed on all GPR signals to increase the sampling rate. Figure 4-5 illustrates an example of the GPR signal before and after interpolation. It can be seen that the original peak location is shifted after the signal is interpolated, which results in a more accurate determination of Δt as shown in Figure 3-3.

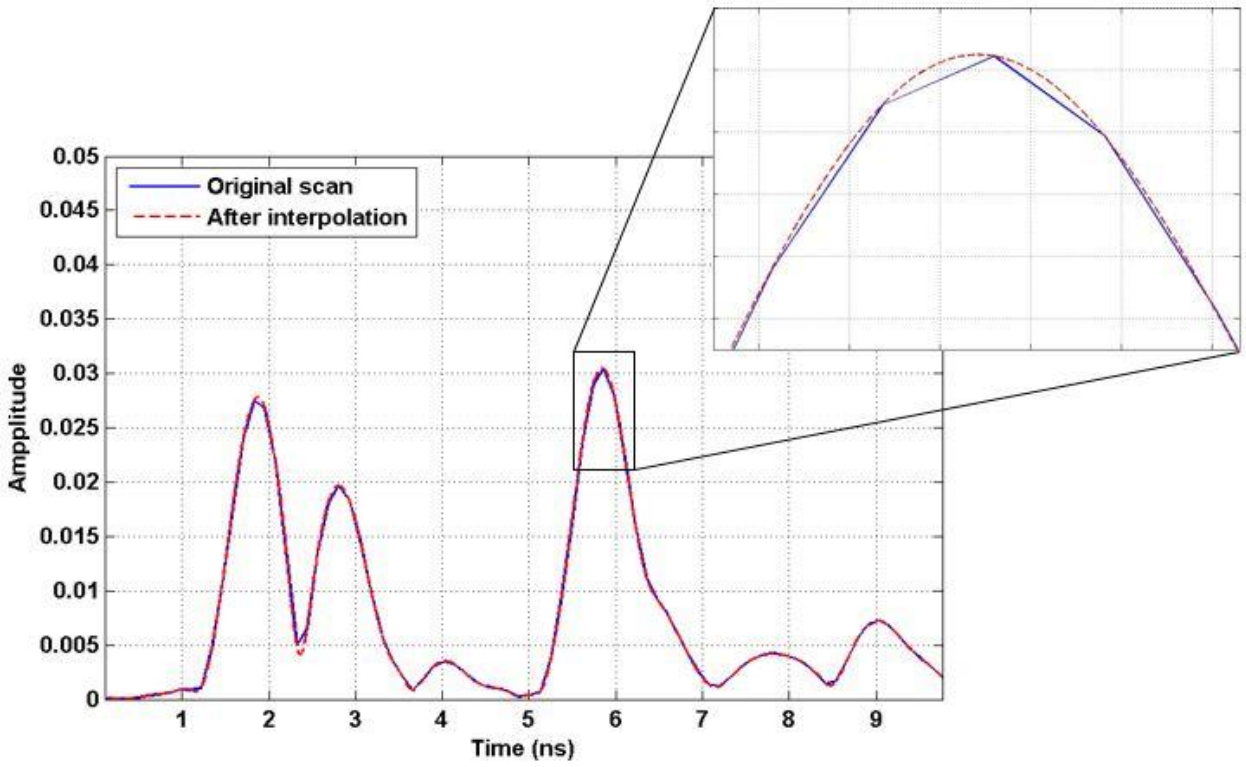

Figure 4-5. Demonstration of 100-point Whittaker–Shannon interpolation on GPR signal

The results of dielectric constants and layer thicknesses from all ten steel plates are shown in Tables 4-6 to 4-9 for all four XCMP test configurations.

Table 4-6. Results for XCMP 1-3 configuration

Steel Plate No.	1	2	3	4	5	6	7	8	9	10
Δt_1 (ns)	0.71	1.95	3.05	1.10	3.92	1.09	2.03	1.04	2.90	1.93
Δt_2 (ns)	0.66	1.97	3.05	1.10	3.91	1.11	2.02	1.03	2.88	1.93
x_1 (m)	-	-	0.060	-	0.083	-	0.043	-	0.091	0.043
x_2 (m)	-	-	0.065	-	0.091	-	0.047	-	0.099	0.047
t_1 (ns)	-	-	3.15	-	4.05	-	2.10	-	3.04	2.00
t_2 (ns)	-	-	3.16	-	4.06	-	2.11	-	3.05	2.01
Dielectric Constant	-	-	7.36	-	6.45	-	6.98	-	4.36	6.66
Thickness (mm)	-	-	172	-	236	-	117	-	214	114

Table 4-7. Results for XCMP 1-5 configuration

Steel Plate No.	1	2	3	4	5	6	7	8	9	10
Δt_1 (ns)	0.72	1.91	3.05	0.93	3.94	1.07	2.07	1.03	2.88	1.95
Δt_2 (ns)	0.66	1.89	3.03	0.91	3.91	1.05	2.05	1.02	2.86	1.94
x_1 (m)	-	0.041	0.062	-	0.062	-	0.044	-	0.059	0.044
x_2 (m)	-	0.051	0.076	-	0.076	-	0.054	-	0.073	0.054
t_1 (ns)	-	1.98	3.15	-	4.04	-	2.14	-	2.98	2.03
t_2 (ns)	-	1.99	3.18	-	4.06	-	2.16	-	3.00	2.04
Dielectric Constant	-	6.88	7.03	-	9.00	-	6.92	-	7.01	6.54
Thickness (mm)	-	111	176	-	200	-	120	-	166	117

Table 4-8. Results for XCMP 1-7 configuration

Steel Plate No.	1	2	3	4	5	6	7	8	9	10
Δt_1 (ns)	0.69	1.95	3.04	0.98	3.89	1.11	2.09	1.04	2.88	1.96
Δt_2 (ns)	0.73	1.92	2.99	0.92	3.83	1.24	2.02	1.05	2.84	1.93
x_1 (m)	-	0.040	0.065	-	0.074	-	0.047	-	0.068	0.038
x_2 (m)	-	0.055	0.090	-	0.104	-	0.063	-	0.095	0.052
t_1 (ns)	-	2.01	3.15	-	4.01	-	2.17	-	3.00	2.02
t_2 (ns)	-	2.04	3.19	-	4.06	-	2.16	-	3.04	2.05
Dielectric Constant	-	7.27	6.68	-	7.27	-	6.61	-	6.03	7.65
Thickness (mm)	-	110	180	-	220	-	124	-	180	108

Table 4-9. Results for XCMP 3-5 configuration

Steel Plate No.	1	2	3	4	5	6	7	8	9	10
Δt_1 (ns)	0.71	1.93	3.04	1.00	3.92	1.06	2.08	1.14	2.89	1.96
Δt_2 (ns)	0.77	1.92	3.03	1.00	3.91	1.03	2.07	1.11	2.86	1.95
x_1 (m)	-	0.039	0.079	-	0.045	-	0.039	-	0.059	0.044
x_2 (m)	-	0.043	0.089	-	0.054	-	0.043	-	0.073	0.049
t_1 (ns)	-	2.00	3.18	-	4.01	-	2.15	-	2.99	2.03
t_2 (ns)	-	2.00	3.20	-	4.02	-	2.16	-	3.01	2.04
Dielectric Constant	-	8.16	5.94	-	7.97	-	8.80	-	4.67	7.27
Thickness (mm)	-	103	192	-	212	-	107	-	206	111

The actual core thicknesses measured in the lab are considered to be the ground truth and are shown in Table 4-10.

Table 4-10. Core thicknesses measured in the lab

Steel Plate No.	1	2	3	4	5	6	7	8	9	10
Thickness (mm)	45	114	178	60	221	64	121	63	165	114

In Tables 4-6 to 4-9, the blank cell represents the core locations where there are no solutions for the four unknowns x_1, x_2, t_1, and t_2 by solving Equations (3-13), (3-14), (3-21) and (3-22), either because Δt_1 and Δt_2 cannot be resolved due to the thin layer thickness, or Δt_1 and Δt_2 are not accurate enough to give the correct answers to x_1, x_2, t_1, and t_2. It is found that for steel plate #1, #4, #6 and #8, all four XCMP configurations give no solutions due to the overlapping of the signals from the surface reflection and the reflection from bottom of the surface layer. This makes sense,

since steel plates #1, #4, #6 and #8 have the thinnest layers; i.e. one lift, or less than 50mm (design thickness) according to Table 4-10. If we assume the average dielectric constant of the asphalt pavement is 7.0, based on the analysis of the 3-D radar signals in Section 3.3.1, the Rayleigh resolution of the EM signal is around 0.61ns, which makes the smallest possible layer thickness that can be resolved $0.61ns \times 3 \times 10^8 m/s \div \sqrt{7} = 69.1mm$. For the XCMP method, the resolution limit is slightly different than 69.1mm depending on the EM wave incident angle.

It can also be noted that in addition to steel plates #1, #4, #6 and #8, the XCMP 1-3 configuration doesn't have a solution for steel plate #2 either. This is because the difference between Δt_1 and Δt_2 is too small: 0.02ns in this case. The value of Δt_i not only dependent on the layer thickness, but also on the offset between the Tx and the Rx. Specifically, for the same layer thickness, the smaller the offset between Tx and Rx, the smaller the value of Δt_i. In order to obtain an accurate solution, we want the difference of Δt_1 and Δt_2 to be as large as possible. Table 4-8 shows that the difference between Δt_1 and Δt_2 is 0.03ns for the XCMP1-7 configuration, which is 50% larger than that of the XCMP1-3 configuration. Theoretically, the performance of the XCMP 1-7 configuration should be better than that of the XCMP 1-5 configuration, and the performance of the XCMP 1-5 configuration should be better than that of the XCMP 1-3 and XCMP 3-5 configurations. This is also the reason why the XCMP 1-3 configuration doesn't have a solution for steel plate #2, although the layer thickness at steel plate #2 is larger than the resolution limit.

In practice, we should use the XCMP configuration with the largest difference between the offset of Tx1/Rx1 and Tx2/Rx2. For example, in the case of the DX1821 antenna array (Figure 3-6), the best XCMP configuration would be XCMP1-21, which uses Tx6/Rx6 as the first antenna

pair, and Tx11/Rx1 as the second antenna pair. However, if multiple line scans are needed, the Tx/Rx offset needs to be less than 21.

Table 4-11 shows the comparison of the prediction error of the results from all four XCMP configurations. To visualize the different performances of the four XCMP configurations, the prediction errors in Table 4-11 are shown in the column chart in Figure 4-6.

Table 4-11. Thickness prediction error (%) from all four XCMP configurations

Steel Plate No.	1	2	3	4	5	6	7	8	9	10	Avg.
XCMP1-3	-	-	3.69	-	6.79	-	2.76	-	29.26	0.40	8.58
XCMP1-5	-	2.40	1.44	-	9.56	-	0.36	-	0.52	2.38	2.85
XCMP1-7	-	3.21	0.75	-	0.45	-	2.95	-	8.74	5.41	3.45
XCMP3-5	-	9.55	7.60	-	4.10	-	11.32	-	24.34	2.62	8.56
Avg.	-	5.05	3.37	-	5.22	-	4.35	-	15.72	2.70	5.86

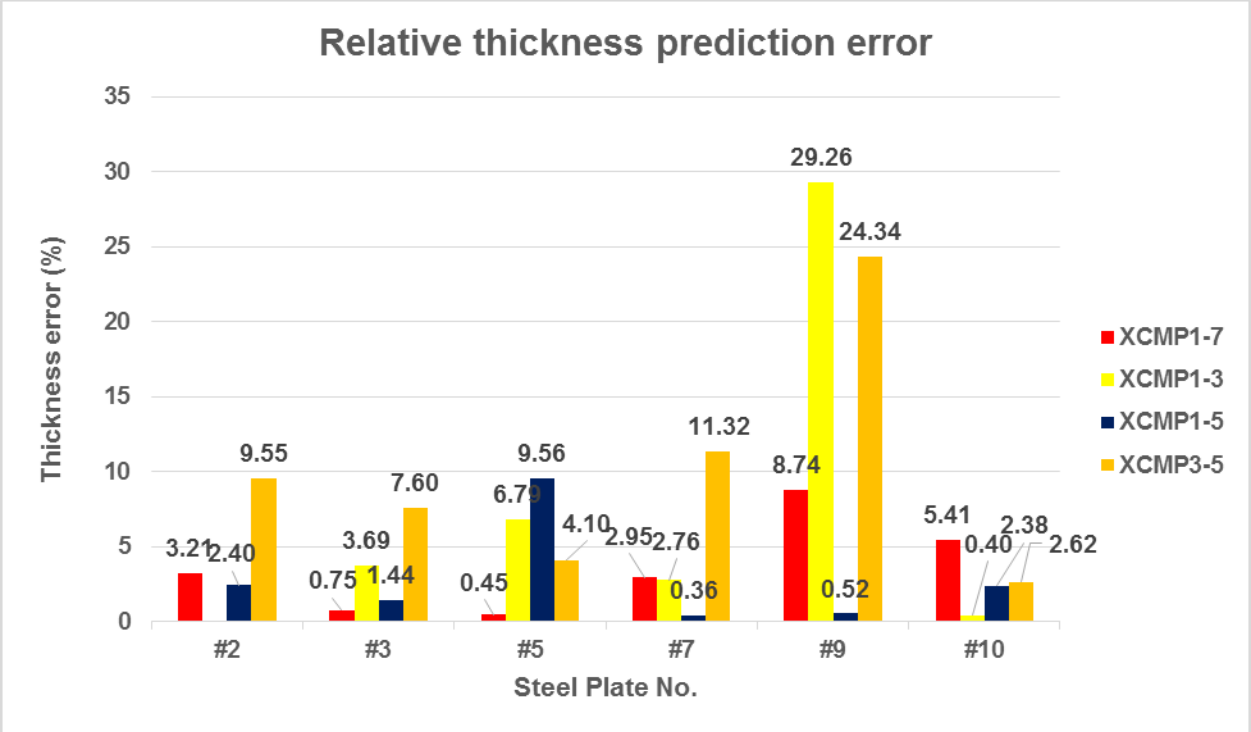

Figure 4-6. Relative thickness prediction errors for all four XCMP configurations

From the results of all XCMP configurations for all ten steel plate locations as shown in Table 4-11 and Figure 4-6, we can first see that the there are no solutions for steel plates #1, #4, #6, and #8. As explained in the previous section, this is because the layer thickness is less than the resolution limit. According to Leng (2011), the 2GHz pulsed radar manufactured by GSSI can provide solutions to all ten steel plate locations, which implies that the time domain resolution of the 2GHz pulsed GPR is better than that of the DX1821 3-D GPR. This was also verified in Section 3.3.1, in which it was shown that the Rayleigh resolution for 2GHz pulsed GPR is 0.54ns, while the Rayleigh resolution for stepped frequency 3-D GPR is only 0.61ns. This observation implies that the bandwidth, which determines the time domain resolution, of the 3-D GPR is not better than that of the 2GHz pulsed GPR, which was expected based on the property of the stepped frequency signal. Therefore, when no super resolution techniques are used, for thin asphalt pavement layers the 2GHz pulsed radar will give a better result. Nonetheless, 3-D GPR has better data collecting speed and survey area coverage, which is extremely important when large areas need to be surveyed; e.g., an airport runway/taxiway. Hence, such information will help to select the best approach for the given conditions.

Sufficient difference between Δt_1 and Δt_2 are required to solve the XCMP equations. The difference between Δt_1 and Δt_2 may be increased by either increasing pavement layer thickness or by increasing the difference between the offsets of the antenna pairs. XCMP1-3 has an insufficient difference between Δt_1 and Δt_2 at steel plate #2 due to combining effect of the small difference between Tx1/Rx1 and Tx2/Rx2. Hence, no solution could be determined.

For steel plates #2, #3, #5, #7, #9, and #10, the average relative thickness prediction errors are 5.05%, 3.37%, 5.22%, 4.35%, 15.72%, and 2.70%, respectively. Excluding steel plate #9, the

maximum average prediction error is 5.22%, which gives an absolute error of 15mm. This value is above the construction tolerance (usually 5mm in the State of Illinois); therefore, not all XCMP configurations are suitable for estimating asphalt pavement thickness for the purposes of QC/QA. The cause of the high prediction error at steel plate #9 is the echoing of the surface reflection (similar to the echoing shown in Figure 4-4), which shifts the second peak of the reflection at the bottom of the surface layer. The echoes could be EM waves bouncing back and forth between the layer interfaces, or between the ground surface and the 3-D GPR antenna structure. This maybe another drawback of the 3-D GPR, since no echoing effects were found in the previous XCMP studies (Leng 2011).

Due to the reasons explained above, XCMP1-5 and XCMP1-7 should be preferred to XCMP1-3 and XCMP3-5. According the Table 4-11, it is confirmed that XCMP1-5 and XCMP1-7 have average relative prediction errors of 2.85% and 3.45%, which are much better than the accuracy of XCMP1-3 and XCMP3-5 (8.58% and 8.56%, respectively). The average absolute error for both XCMP1-5 and XCMP1-7 configurations is 5mm, which meets the construction tolerance.

It should be noted that XCMP can be used to obtain the dielectric constant of asphalt concrete. Specifically, if the dielectric constant is constant throughout the pavement, average dielectric constant values may be obtained from various locations. The averaging process will eliminate random errors such as those due to the echoing effect. Using averaged dielectric constant and traditional two-way travel time method, an accurate thickness profile may be obtained. In this case, the nondestructive XCMP method serves the same purpose as the dielectric constant calibration by taking cores. The XCMP also provides greater area coverage.

4.3 Summary

To measure the asphalt pavement thickness using GPR, the CMP method is preferred to the traditional two-way travel time method, as it can be used without calibrating the dielectric constant. XCMP method is an extended CMP method that can use two air-coupled antenna pairs to conduct the study without using additional ground-coupled antenna pairs. The advantage of using air-coupled antennas is that they allow to collect GPR data at highway speeds, making it possible to survey a large area. In this study, a DX 1821 3-D GPR was used to conduct the XCMP method.

A test site was built with various thicknesses (ranging from one lift to four lifts), and ten steel plates are embedded under each of the asphalt lifts. A standard test pattern along with 4 XCMP configurations—XCMP1-3, XCMP1-5, XCMP1-7, and XCMP3-5—are designed to evaluate the performance of different XCMP configurations.

From the collected data of the standard test pattern, we found that by selecting horizontal slices at different depths, the steel plates embedded under each lift can be clearly detected. The echoing effects can be seen from the longitudinal vertical slices. By integrating all the data collected from 3-D GPR, a 3-D map can be generated.

For the XCMP method, the data reflected from each of the steel plates are used due to the large reflection from the steel plates. Whittaker-Shannon interpolation was performed on the GPR signals to increase the time domain sampling rate. The XCMP equations are numerically solved using least squares. Cores were taken at each of the steel plates' locations to obtain the true layer thickness as ground truth. From the data of the four XCMP configurations, it could be concluded that the time domain resolution of the 3-D GPR is not enough for layers thinner than 50mm. Another valuable point is that XCMP1-5 and XCMO1-7 performs better than XCMP1-3 and

XCMP3-5. Overall, the average thickness prediction error for layers thicker than 50mm is 5mm, which is within the construction tolerance.

CHAPTER 5: FINDINGS, CONCLUSIONS, AND RECOMMENDATIONS

5.1 Summary

Layer thickness is one of the most important parts of asphalt concrete pavement and one of the most important parameters in pavement design, since it largely determines the pavement load capacity. Layer thickness also plays a critical role in the pavement rehabilitation strategy. For existing pavement, it is an important factor that predicts the condition of the pavement and its remaining service life. For newly built flexible pavement, the layer thickness is used for QC/QA. Coring has been predominantly used by agencies to obtain the asphalt layer thickness. However, it is destructive and can only provide data at limited locations. The use of GPR to estimate the asphalt pavement layer thickness has been studied for many years and has become the most prevalent application of GPR in civil engineering. The major difficulty in the application is the inaccuracy of determining the dielectric constant and the requirement of dielectric constant calibration by taking cores. The XCMP method is an alternative to the traditional two-way travel time method, and it can provide more accurate dielectric constant values without calibration. This study attempts to integrate the XCMP method with a stepped-frequency antenna array—3-D GPR—by developing signal processing techniques and numerical analysis methods.

A full-scale asphalt concrete test lane was utilized to evaluate the performance of the XCMP method with 3-D GPR. The thickness of the asphalt pavement ranged from one lift to four lifts (each lift is around 50.8mm thick). Steel plates were embedded under 10 locations with different layer thicknesses to increase the reflection amplitude. Five 3-D GPR configurations were designed: one standard scan patter, XCMP1-3, XCMP1-5, XCMP1-7, and XCMP3-5. A Whittaker-Shannon interpolation algorithm was developed to increase the time domain sampling

rate, which is important to solving the XCMP equations. A numerical solving technique based on least square principle was introduced to solve the XCMP equations.

The introduced algorithm was used on the GPR signal reflected from ten steel plates. Cores were taken at each of the steel plate locations and their lab-measured thicknesses were chosen as the ground truth. A comparison of the XCMP measured thickness with the ground truth shows that 3-D GPR can be used together with the XCMP method to estimate asphalt layer thickness with good data acquisition speed and large coverage area.

5.2 Findings

The findings of this study are summarized as following:

- The time domain sampling interval of the 3-D GPR is 0.12207 ns, which is smaller than that of the 2GHz pulsed antenna. Since the accurate determination of Δt_i is essential for the XCMP algorithm, the Whittaker-Shannon interpolation can be used to increase the time domain sampling rate. The interpolated signal was used in the XCMP method and reasonable results were obtained.
- The four XCMP equations can be solved numerically utilizing the least square error approach. Constraints need to be set based on the physical representation of the variables to ensure robustness of the outcome.
- The Rayleigh resolution of stepped-frequency DX1821 3-D GPR is 0.62ns, which is smaller than that of the 2GHz pulsed GPR. For asphalt pavement thinner than 50mm, the time domain resolution of the 3-D GPR is inadequate. Accordingly, the bandwidth of the stepped-frequency DX1821 3-D GPR is smaller than that of the 2GHz pulsed GPR.

- The echo presence of the surface reflection can be overlapped with the reflection from the bottom of the surface layer, resulting in inaccurate XCMP results.
- As the difference between Δt_1 and Δt_2 in the XCMP is larger, the higher the accuracy.
- The average thickness estimation error for both XCMP1-5 and XCMP1-7 is 5mm, which meets the construction tolerance. Therefore, in practice, XCMP1-5 and XCMP1-7 are suitable for QA/QC of asphalt pavement thicker than 50mm.

5.3 Conclusions

Based on the results of the study, the following conclusions can be drawn:

- Accurate determination of Δt_1 and Δt_2 are critical in the XCMP method. Whittaker-Shannon interpolation can be applied to the 3-D GPR signals to increase the time domain sampling rate.
- XCMP algorithms with large difference between the offsets of the two antenna pairs be can be used to estimate the thickness of asphalt layers which are thicker than 50mm without calibration of dielectric constant. The average thickness estimation error is 5mm, which is within construction tolerance.The data collection speed of DX1821 3-D GPR is 21 times faster than that of the typical horn antenna. Therefore, 3-D GPR may be used in large survey areas such as airport runways/taxiways to generate a two-dimensional thickness profile or to identify possible pavement flaws.

5.4 Recommendations

This study shows the feasibility of 3-D GPR to estimate asphalt pavement thickness using the XCMP method. As a continuation of the study, the recommendations for future study are as follows:

- For asphalt pavement thinner than 50mm, the current 3-D GPR system doesn't have enough time domain resolution. Therefore super-resolution techniques are needed to estimate thin layer thickness.
- Effect of asphalt surface moisture on 3-D GPR signal needs to be investigated.
- Since echoing effect affects the accurate determination of Δt_1 and Δt_2 , it is necessary to introduce signal processing techniques to eliminate the effect of surface reflection echoes.
- The performance of other 3-D GPR models should be studied.

References

3D-Radar GPR. 2015. http://www.3d-radar.com/.

Al-Qadi, I. L., Ghodgaonkar D., Varada V., and Varadan V., 1991. "Effect of Moisture on Asphaltic Concrete at Microwave Frequencies." *IEEE Transactions on Geoscience and Remote Sensing*, 29.5, 710-717.

Al-Qadi, I., Lahouar S., and Loulizi A., 2001. "In Situ Measurements of Hot-Mix Asphalt Dielectric Properties." *NDT & E International*, 34.6, 427-434.

Al-Qadi, I., Lahouar S., and Loulizi. A., 2003. "Successful Application of Ground-Penetrating Radar for Quality Assurance-Quality Control of New Pavements." *Transportation Research Record: Journal of the Transportation Research Board*, 1861.1, 86-97.

Al-Qadi, I., and Lahouar S., 2005. "Measuring Layer Thicknesses with GPR–Theory to Practice." *Construction and Building Materials*, 19.10, 763-772.

Al-Qadi, I.L., Leng Z., Lahouar S., Baek J., 2010. "In-place hot-mix asphalt density estimation using ground-penetrating radar." *Transportation Research Record: Journal of the Transportation Research Board*, 2152.1, 19-27.

ASTM D6432 - 11. "Standard Guide for using the Surface Ground Penetrating Radar Method for Subsurface Investigation."

Blahut, Richard E., 2004. *Theory of remote image formation*. Cambridge University Press.

Claessen, A. I. M., Edwards J. M., Sommer P., and Uge P., 1977. "Asphalt Pavement Design--The Shell Method." In Volume I of proceedings of 4th International Conference on Structural Design of Asphalt Pavements, Ann Arbor, Michigan, August 22-26, 1977 (No. Proceeding).

Culick, F. E. C., 1987. "A note on Rayleigh's criterion." *Combustion Science and Technology*, 56. 4-6, 159-166.

Chang, C. W., Lin C. H., and Lien H. S., 2009. "Measurement Radius of Reinforcing Steel Bar in 5 Concrete using Digital Image GPR." *Construction and Building Materials*, 23.2, 1057-1063.

Chuang, S. L., 2012. *Physics of photonic devices*. 80. John Wiley & Sons.

Daniels, David J., 2005. *Ground penetrating radar*. John Wiley & Sons, Inc.

Eide, Egil S., 2000. "Ultra-wideband transmit/receive antenna pair for ground penetrating radar." *IEE Proceedings-Microwaves, Antennas and Propagation*, 147.3, 231-235.

Eide, E. S., and Jens F. H., 2002. "3D utility mapping using electronically scanned antenna array." Ninth International Conference on Ground Penetrating Radar (GPR2002), International Society for Optics and Photonics.

Eide, E., and Sala J., 2012. High Resolution Step-Frequency 3D GPR Using Wideband Antenna Arrays (Presentation at Seminar of Ground Penetrating Radar in Road Monitoring and Evaluation Now and the Future).

Huang, Y. H., 1993. *Pavement analysis and design*. Transportation Research Board.

Huisman, J., Sperl C., Bouten W., and Verstraten J., 2001. "Soil Water Content Measurements at Different Scales: Accuracy of Time Domain Reflectometry and Ground-Penetrating Radar." *Journal of Hydrology,* 245.1, 48-58.

IEEE Standard 145-1993, 1993. *IEEE Standard Definitions of Terms for Antennas*.

Jin, Jian-Ming., 2011. *Theory and computation of electromagnetic fields*. John Wiley & Sons.

Jol, Harry M., ed., 2008. *Ground penetrating radar theory and applications*. Elsevier.

Kassem, E., Scullion T., Masad E., and Chowdhury A., 2012. "Comprehensive Evaluation of Compaction of Asphalt Pavements and a Practical Approach for Density Predictions." *Transportation Research Record: Journal of the Transportation Research Board*, 2268.1, 98–107.

Lahouar, S., Al-Qadi I., Loulizi A., Clark T., and Lee D., 2002. "Approach to Determining in Situ Dielectric Constant of Pavements: Development and Implementation at Interstate 81 in Virginia." *Transportation Research Record: Journal of the Transportation Research Board*. 1806.1, 81-87.

Lahouar, S., 2003. "Development of data analysis algorithms for interpretation of ground penetrating radar data (Doctoral dissertation, Virginia Polytechnic Institute and State University)."

Le Bastard, C., Baltazart V., Derobert X., and Wang Y., 2012. "Support Vector Regression method applied to thin pavement thickness estimation by GPR." *Ground Penetrating Radar (GPR), 2012 14th International Conference on IEEE*, 349-353.

Leckebusch, J., 2011. "Comparison of a stepped‐frequency continuous wave and a pulsed GPR system." *Archaeological Prospection*, 18.1, 15-25.

Leng, Z., Al-Qadi I.L., Lahouar S., 2011. "Development and validation for in situ asphalt mixture density prediction models." *NDT & E International*, 44, 369-375.

Leng, Z., 2011. "Prediction of in-situ asphalt mixture density using ground penetrating radar: theoretical development and field verification (Doctoral dissertation, University of Illinois at Urbana-Champaign)."

Leng, Z., Al-Qadi, I. L., Shangguan P., Son S., 2012. "Field application of ground penetrating radar for asphalt mixture density measurement: a case study of Illinois Route 72 Overlay." *Transportation Research Record: Journal of the Transportation Research Board*, 2304, 133–141.

Leng, Z., and Al-Qadi I. L., 2014. "An innovative method for measuring pavement dielectric constant using the extended CMP method with two air-coupled GPR systems." *NDT & E International*, 66, 90-98.

Liu, H., Takahashi K., and Sato M., 2014. "Measurement of Dielectric Permittivity and Thickness of Snow and Ice on a Brackish Lagoon using GPR." *IEEE Journal of Selected Topics in Applied Earth Observations and Remote Sensing*, 7.3, 820-827.

Liu, H., and Sato M., 2014. "In Situ Measurement of Pavement Thickness and Dielectric Permittivity by GPR using an Antenna Array." *NDT & E International*, 64, 65-71.

Lyons, Richard G., 2010. *Understanding digital signal processing.* Pearson Education.

Masad, E., Al-Rub R. A., and Little D. N., 2012. "Recent Developments and Applications of Pavement Analysis Using Nonlinear Damage (PANDA) Model." In 7th RILEM International Conference on Cracking in Pavements (pp. 399-408). Springer Netherlands.

Morey, R. M., 1998. *Ground Penetrating Radar for Evaluating Subsurface Conditions for Transportation Facilities.* Transportation Research Board.

Roberts, F. L., Kandhal P. S., Brown E. R., Lee D.Y., and Kennedy T. W., 1996. "Hot mix asphalt materials, mixture design and construction."

Saarenketo, T., 1997. "Using ground-penetrating radar and dielectric probe measurements in pavement density quality control." *Transportation Research Record: Journal of the Transportation Research Board*, 1575.1, 34-41.

Saarenketo, T., and Scullion T., 2000. "Road Evaluation with Ground Penetrating Radar." *Journal of Applied Geophysics*, 43.2-4, 119–138.

Schneider, W. A., 1984. "The common depth point stack." *Proceedings of the IEEE*, 72.10, 1238-1254.

Shangguan, P., Al-Qadi I., Coenen A., and Zhao S., 2014a. "Algorithm development for the application of ground-penetrating radar on asphalt pavement compaction monitoring." *International Journal of Pavement Engineering*, 1-12.

Shangguan, P., and Al-Qadi, I. L., 2014b. "Calibration of FDTD simulation of GPR signal for asphalt pavement compaction monitoring." *IEEE Transactions on Geoscience and Remote Sensing*, 53.3, 1538-1548.

Shangguan, P., 2015. "Development of algorithms for asphalt pavement compaction monitoring utilizing ground penetrating radar." Diss. University of Illinois at Urbana-Champaign.

Stutzman, W. L., and Thiele G. A., 2012. *Antenna theory and design*. John Wiley & Sons.

Uda, S. 1928. "On the Wireless Beam of Short Electric Waves". Institute of Electrical Engineers of Japan.

Yilmaz, Ö., 2008. "Seismic data analysis: processing, inversion, and interpretation of seismic data." *Tulsa: Society of Exploration Geophysicists*.

Yoder, E. J., and Witczak M. W., 1975. *Principles of pavement design*. John Wiley & Sons.

Zhao, S., Shangguan P., and Al-Qadi I., 2015. "Application of Regularized Deconvolution Technique for Predicting Pavement Thin Layer Thicknesses from Ground Penetrating Radar Data." *NDT & E International*, 73, 1-7.